Simultaneous individual and dipolar collective properties in binary assemblies of magnetic nanoparticles

Elena H. Sánchez[1*], *Marianna Vasilakaki*[2], *Su Seong Lee*[3], *Peter S. Normile*[1], *Giuseppe Muscas*[4], *Massimiliano Murgia*[1,5], *Mikael S. Andersson*[6,7], *Gurvinder Singh*[8], *Roland Mathieu*[6], *Per Nordblad*[6], *Pier Carlo Ricci*[5], *Davide Peddis*[9,10], *Kalliopi N. Trohidou*[2], *Josep Nogués*[11,12*], *José A. De Toro*[1*]

[1] Instituto Regional de Investigación Científica Aplicada (IRICA) and Departamento de Física Aplicada, Universidad de Castilla-La Mancha 13071 Ciudad Real, Spain

[2] Institute of Nanoscience and Nanotechnology, NCSR "Demokritos", 153 10 Agia Paraskevi, Attiki, Greece

[3] Institute of Bioengineering and Nanotechnology, 31 Biopolis Way, The Nanos, Singapore 138669, Singapore

[4] Department of Physics and Astronomy, Uppsala University, Box 516, SE-751 20, Uppsala, Sweden

[5] Dipartimento di Fisica, Universitá degli Studi di Cagliari, S.P. Monserrato-Sestu Km 0,700, 09042 Monserrato (CA), Italy

[6] Department of Engineering Sciences, Uppsala University, Box 534, SE-751 21 Uppsala, Sweden

[7] Department of Chemistry and Chemical Engineering, Chalmers University of Technology, SE-412 96 Göteborg, Sweden

[8] School of Aerospace, Mechanical and Mechatronic Engineering, University of Sydney, Sydney, NSW 2008, Australia

[9]Università degli Studi di Genova, Dipartimento di Chimica e Chimica Industriale, Via Dodecaneso 31, 1-16146 Genova, Italy

[10]Istituto di Structura della Materia-CNR, 00015 Monterotondo Scalo (RM), Italy

[11] Catalan Institute of Nanoscience and Nanotechnology (ICN2), CSIC and BIST, Campus UAB, Bellaterra, 08193 Barcelona, Spain

[12] ICREA, Pg. Lluís Companys 23, 08010 Barcelona, Spain

ABSTRACT

Applications based on aggregates of magnetic nanoparticles are becoming increasingly widespread, ranging from hyperthermia to magnetic recording. However, although some uses require a collective behavior, other need a more individual-like response, the conditions leading to either of these behaviors are still poorly understood. Here we use nanoscale-uniform binary random dense mixtures with different proportions of oxide magnetic nanoparticles with low/high anisotropy as a valuable tool to explore the crossover from individual to collective behavior. Two different *anisotropy scenarios* have been studied in two series of binary compacts: M1, comprising maghemite (γ-Fe_2O_3) nanoparticles of different sizes (9.0 nm / 11.5 nm) with barely a factor of 2 between their anisotropy energies, and M2, mixing equally-sized pure maghemite (low-anisotropy) and Co-doped maghemite (high-anisotropy) nanoparticles with a large difference in anisotropy energy (ratio > 8). Interestingly, while the M1 series exhibits collective behavior typical of strongly-coupled dipolar systems, the M2 series presents a more complex scenario where different magnetic properties resemble either "individual-like" or "collective", crucially emphasizing that the *collective* character must be ascribed to specific properties and not to the system as a whole. The strong differences between the two series, offer new insight (systematically ratified by simulations) into the subtle interplay between dipolar interactions, local anisotropy and sample heterogeneity, to determine the behavior of dense assemblies of magnetic nanoparticles.

INTRODUCTION

Dense nanoparticle (NP) assemblies are the basis of an ever-increasing catalogue of applications.[1–4] The advances in synthetic chemistry have allowed the preparation of monodisperse, highly uniform NPs, which in turn has enabled their assembly to build NP analogues of atomic crystals (sometimes called super- or supra-crystals/lattices), either comprising a single type of NP,[5–11] or several species to form supra-compounds exhibiting a remarkable variety of crystal symmetries.[12–15] However, the most studied NP composite systems are disordered mixtures pursuing a combination of properties to optimize a given figure of merit. For instance, in the broad field of nanomagnetism the idea is epitomized by the exchange-coupling strategy between magnetically soft and hard nanograins (with high saturation magnetization and large coercivity, respectively) in order to maximize the energy product of novel permanent magnets.[16–20] These composites are typically metallic and the ferromagnetic grains interact *via* direct exchange, leading to single-phase behavior with enhanced properties.[19–21] On the other hand, compacts of oxide nanoparticles, where the interparticle interactions are mainly of dipole-dipole type, typically show superspin glass behavior[22–24] (previously described for dipolarly-interacting dense ferrofluids[25]).

Collective behavior in magnetic nanoparticle systems can be useful for some applications like hyperthermia and magnetic resonance imaging.[26,27] In the recently-discovered "liquid permanent magnets" based on nanoparticles, strong dipolar interactions are crucial to enhance the thermal stability of the magnetization and transform the droplet surface into a ferromagnetic layer.[28] On the other hand, collective behavior, or even short-range correlations, is detrimental for the performance of magnetic nanoparticles/grains in magnetic storage and magnetoresistance sensing.[29,30] Thus, understanding the collective vs individual behavior of dense systems of nanoparticles becomes crucial to optimize those applications. Although *collective* behavior is a fundamental term in condensed matter physics[31] or any other type of complex network,[32] its meaning is not clear-cut in the context of magnetic nanoparticle systems, where the differentiation between modified-single-particle behavior and collective order driven by dipolar interactions has produced a large body of experimental and theoretical literature.[33–39] In general, the term *collective* is intended to describe the emergence of patterns of large-scale behavior from the complex interactions between small constituent parts. However, different properties are determined at different length scales, prompting the possibility for a given system to exhibit both individual and collective properties. In this context, dense binary assemblies are presented here as a unique tool to shed light on the above ideas, as in these systems "individual" properties will be evidenced by a doublet of values, each corresponding to one type of constituent.

In binary NP composites nanoscale homogeneity is crucial to enable the tuning of the properties beyond that of the simple superposition of the two constituents.[14,15,40–42] Notably, although binary random compacts of oxide NPs, where the local anisotropy can be readily tuned by the proportion of high/low anisotropy particles in the mix, offer the possibility to explore the complex relation between interparticle interactions and local anisotropy, this tool has been very rarely employed to address the issue.[40] Here, exploiting the narrow size distribution of the constituent particles (2% polydispersity), we have prepared what could be considered the simplest possible NP composites by randomly mixing and compacting two populations of NPs with different anisotropy energy barriers. Two complementary series of such mixtures have been prepared with a moderate/large difference in the anisotropy energy of the constituent NPs. The results show that the proportion of low and high anisotropy (LA, HA) particles in these highly homogeneous compacts may be used to fine tune both the hysteresis loops and the low-field magnetization dynamics (e.g., the blocking/freezing temperature) of the assemblies. Moreover, our experiments allow an assessment of the weight of single-particle *versus* dipolar interaction energies in the determination of the above magnetic properties, with contrasting results between the two series studied.

RESULTS AND DISCUSSION

The M1 and M2 series of binary compacts were prepared mixing in different proportions highly uniform, roughly spherical, maghemite-based NPs with different size and different anisotropy constant, respectively (see Methods). The particles were mixed while still in liquid solution, which was subsequently dried up, and -after washing out the oleic acid surfactant- the resulting powder was compacted to form dense discs [see inset in Figure 1(c)]. For the M1 series, NPs with mean diameters $d_{\mathrm{TEM}} = 9.0$ and 11.5 nm (corresponding to a volume ratio of 2) were used [Figure 1(a), (b) and (d)]. For M2, equally-sized, 6.8 nm, pure and Co-doped maghemite NPs were mixed [Figure 1(e) and (f)]. The samples are denoted as Mi-x, where $i = 1, 2$ refers to the series and $x = 0, 10, 20, 30, 50, 65, 85, 100\%$ in both series (x, defined as the proportion of HA particles). The uniform mixing of the NPs, down to the particle level, was verified by high resolution scanning electron microscope (HRSEM) images in the case of the M1 series [Figure 1(c)],[43] and by compositional mapping for the M2 series, where the mixed nanoparticles have the same size but different composition [Figure 1(g) and (h)].

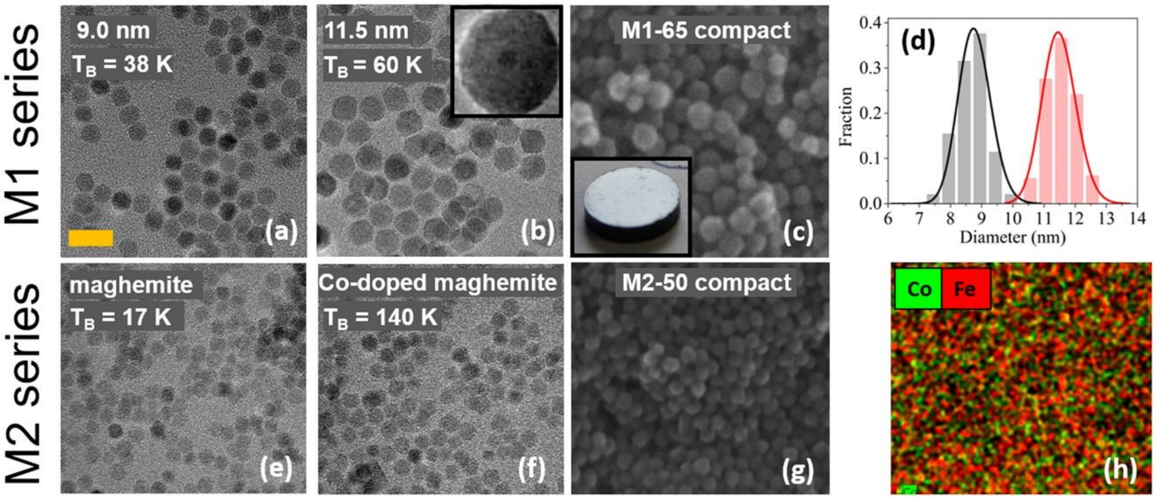

Figure 1. TEM images of the 9 nm (a) and 11.5 nm (b) particles used to prepare the M1-*x* samples. The inset in (b) shows a silica coated 11.5 nm maghemite nanoparticle. (c) Typical HRSEM image of a compact in the M1 series (x = 65), showing the nanoscale mixing of small and large particles. The inset shows one of the discs compacted under 1 GPa. (d) Size distributions of both types of particles. (e, f) TEM images of the 6.8 nm maghemite (e) and Co-doped maghemite (f) particles mixed in the M2 series. SEM image (g) and compositional mapping (h) of M2-50 proving the nanoscale mixing. All the images are scaled (orange scale bar = 20 nm). The TEM images in (a), (b), (e) and (f) were taken in the unmixed suspensions before removing the oleic acid coating. Note also that T_B in the labels of panels (a), (b), (e) and (f) refers to the blocking temperature (defined as the peak temperature of the ZFC curve) of the isolated NPs (silica-coated).

In addition, a fraction of the four types of NPs was extracted from each batch to be coated with a thick silica shell [$t \approx 3d_{\mathrm{TEM}}$; see *e.g.*, inset in Figure 1(b)] in order to magnetically isolate the cores and thus measure the single-particle magnetic properties.[23,44] Each type of nanoparticle is characterized by an energy barrier $K_{ef}V$, where K_{ef} is the effective anisotropy and V is the particle volume, which is directly proportional to the blocking temperature, T_B [taken here simply as the peak temperature in the zero-field-cooled, ZFC, magnetization curve, see Figure 2(a)], of the individual nanoparticles, $T_B \propto K_{ef}V$. Thus, the ratio of T_B's of the isolated nanoparticles quantifies the difference in energy barriers between the two types of particles. Therefore, we define an *anisotropy energy contrast*, AEC, as the ratio of the blocking temperatures of the two types of particles in the composite, $T_{B,HA}/T_{B,LA}$. Following this definition, the M1 series has a moderate AEC $\approx$ 1.6 [where the larger surface anisotropy contribution to K_{ef} in the smaller particles explains the AEC < 2 (particles volume ratio)[45]], while the M2 series is characterized by a much larger AEC $\approx$ 8.2 (due to the large increase in anisotropy caused by the Co-doping of the maghemite particles).[46] Note that although the ZFC curve peak position systematically and significantly overestimates the blocking temperature,[47,48] the AEC is defined as the ratio of the T_B's of the different components and, therefore, is barely affected by this approximation (see Supporting Information, SI).

Figure 2(a) displays the ZFC curves measured in dilute systems (magnetic cores separated by thick silica shells) of the nanoparticles employed to prepare the M1 and M2 mixtures. The different AEC ratios translate, through the Arrhenius exponential dependence of the relaxation time on the energy barrier [see Figure 2(b)], into enormous differences in the individual dynamics of the particles making up the M2 mixtures [e.g., a factor ~10^{10} at T = 150 K, see inset in Figure 2(b)], whereas for the M1 series such differences are comparatively modest (e.g., only a factor ~ 70 at T = 150 K).

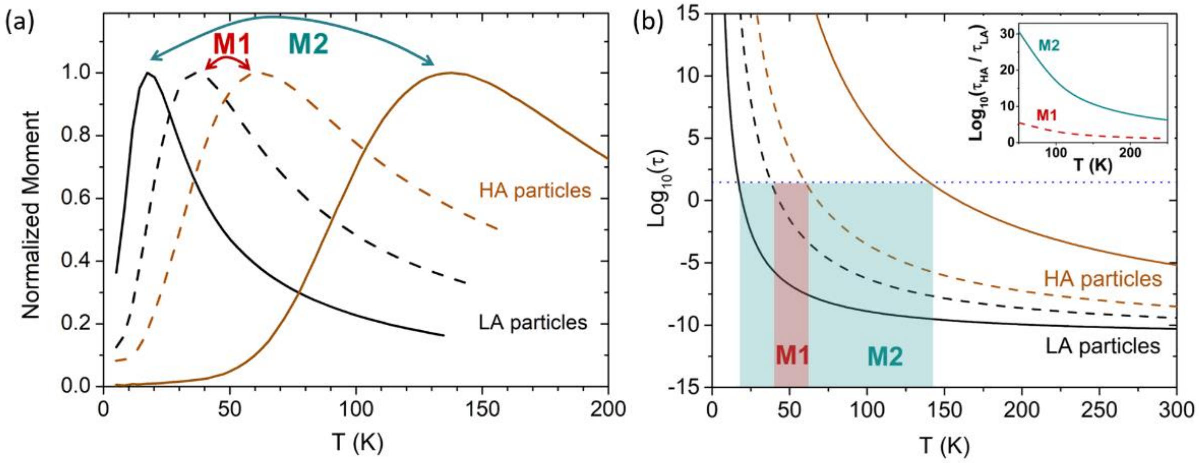

Figure 2. (a) Normalized ZFC magnetization curves measured (in H = 5 Oe) in dilute dispersions of the LA/HA magnetic particles (black/brown curves) employed to prepare the compact mixtures of series M1 (dashed lines) and series M2 (solid lines). (b) Temperature evolution of the relaxation time (Arrhenius law) of the isolated LA/HA particles, considering $\tau_0 = 10^{-11}$ s and the blocking temperatures indicated in panel (a). The horizontal line marks the typical observation times in dc measurements (τ_{obs} ~ 30 s). The different width of the colored boxes emphasizes the difference in "anisotropy energy contrast" between series M1 and M2. The inset shows the temperature dependence of the ratio of relaxation times of the constituent particles for both series.

The ZFC curves measured for all the M1 and M2 binary compacts are shown in Figure 3. In both series there appears a single peak in the M(T) at $T_{MAX,}$ suggesting that dipolar interparticle interactions (see SI, for a discussion on the nature of interparticle interactions)[49] are strong enough to provide collective behavior in the dense assemblies (*cf.* the superposition curves, corresponding to unmixed compacts, shown in Figure S1). In the M1 series the T_{MAX} values are much higher than the individual blocking temperatures of both the LA and HA particles. This is consistent with the flat shape of the FC curve below the freezing temperature [as exemplified in the inset of Figure 3(a) for one of the composites], typical of strongly interacting particle systems. Note that although all samples freeze cooperatively at a single transition temperature, the broader effective size distribution in the central members of the series (as well as the demagnetizing field due to the disc shape in *all* samples)[50] smears out the transition.[51] On the other hand, for the M2 series, although the T_{MAX} values are still higher than the blocking temperature of the hard NP (140 K), the increase is relatively small compared to the M1 series, hinting an important role for the particle anisotropy -and the particles anisotropy contrast- despite the single ZFC peak in the compacts. In fact, the ZFC curves also show a hump at low temperatures ($T \approx 30$ K), except for the end members [see Figure 3(b)], a feature that can be more clearly observed in ac susceptibility measurements (see Figure S2). Notably, this effect is absent in the M1 series.

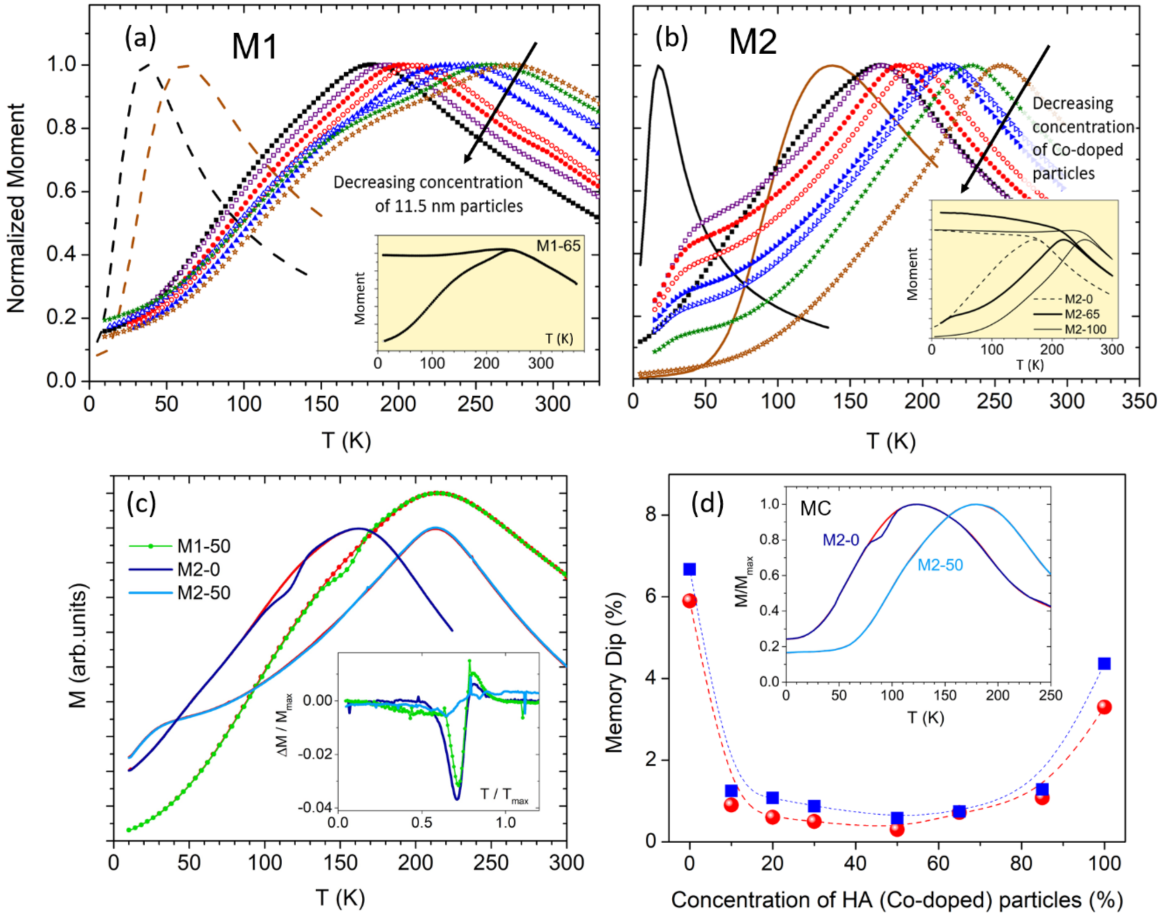

Figure 3. (a) and (b): ZFC normalized magnetization (M/M$_{MAX}$) curves measured in H = 5 Oe for the two series of compacts, as well as for the LA/HA particles isolated by silica spacers also plotted in Figure 2(a). The insets show the field-cooled and ZFC curves for one of the mixtures of series M1 (all samples in this series showed a very similar behavior) and for the end members as well as one of the mixtures in the M2 series. (c): ZFC memory experiments for M1-50, M2-0 and M2-50. The reference curves measured without a halt are plotted with red lines and the memory ZFC curves measured after a halt at $T_{halt} = 2 \cdot T_{MAX}/3$ are plotted with a green line for M1-50, a dark blue line for M2-0 and a light blue line for M2-50. The corresponding difference curves are plotted as a function of the

reduced temperature T/T_{MAX} in the inset. (d): Dependence on the concentration of HA particles of the ZFC memory dip in the M2 series, experimental (red circles) and Monte Carlo (blue squares) results. The inset shows two examples of simulated ZFC memory experiments (M2-0 and M2-50 systems).

To get a deeper understanding on the dynamical properties of the samples, we have looked for a fingerprint of low-field collective behavior, namely the *ageing* and *rejuvenation* (leading to the ZFC *memory* effect) characteristic of spin glasses[24,52,53] and *superspin glasses*, a state customarily observed at low temperature in strongly dipolar-interacting systems.[22,54,55] The memory effect manifests as a dip[52,53] (with respect to a reference ZFC curve) at the halt temperature T_{halt} in a ZFC "memory" curve measured in exactly the same conditions as the reference except for a halt at T_{halt} during the zero-field cooling (see Methods). Remarkably, for the M2 series, we found that, although the end members of the series show a strong memory effect, this phenomenon is essentially suppressed in all the mixtures [see Figure 3(d)], as exemplified in Figure 3(c) for the M2-50 sample. In contrast, all the samples in the M1 series show strong ZFC memory effects, as can be seen also in Figure 3(c) for the most unfavorable case, the M1-50 sample. Although still robust, the weaker memory effect in M2-100 compared to M2-0 is analogous to observations in conventional (atomic) spin glasses, where increasing spin anisotropies were shown to yield weaker memory effects.[56] On the other hand, the severe reduction of the memory effect with the introduction of even a small proportion of a (softer/harder) second phase, and its virtually complete suppression for the central sample of the series (M2-50), is rather unexpected and highlights the crucial role of heterogeneity in the zero-field dynamics.

This result was consequently explored by Monte Carlo simulations using a three-spin model,[57] based on bulk parameters and the experimental results, for particles interacting exclusively through dipole-dipole interactions (see SI for details of the model). The simulations reproduced precisely the experimental results [see Figure 3(d), blue data points and example ZFC curves in the inset], both qualitatively (suppression of the effect upon mixing) and quantitatively (the values of the memory dip relative to the reference ZFC magnetization at T_{halt}). In the model, the strong anisotropy contrast between the two types of simulated nanoparticle samples and the interplay between nanoparticle anisotropy, including the surface contribution, and interparticle interactions result in the observed memory effects.

The humps in the M(T) and the absence of memory effects in the M2 series are related to the difference in relaxation times of the pure and Co-doped particles [see Figure 2(b)]. Namely, the Co-doped particles are essentially blocked in the temperature range of the low temperature hump in the ZFC curves at the observation times of the experiments (~30 s for SQUID magnetization measurements). Thus, these particles act as weak static random fields, which are not able to participate in the dynamics of the system. In the M2-0 and M2-100, all the particles are equal, thus they all participate in the collective (equilibrium and non-equilibrium) dynamics. In the M2 mixtures, however, the blocked Co-doped particles affect the evolution towards an equilibrium phase and leave a fraction of the soft maghemite particles (not always the same) as quasi-superparamagnetic, yielding the low-temperature anomaly. Moreover, due to the much longer relaxation times of the Co-doped nanoparticles, they act as disturbances in the evolution towards equilibrium dynamics in the memory experiments. This implies that the system essentially remains in a non-equilibrium state in all time scales, thus the experiments probe non-equilibrium dynamics, which should have weaker memory effects. On the other hand, in the M1 series the relaxation times of the two types of particles are similar [dashed lines in Figure 2(b)], consequently, the dynamics of the different samples is more homogeneous leading to memory effects and the absence of a low temperature hump in M(T) for the whole series. Therefore, the presence of a single peak at T_{MAX} in the ZFC curve measured in the mixtures, although resulting from strong enough interactions, does not necessarily imply single-phase dynamics below such peak temperature.

This heterogeneity-driven suppression of the collective relaxation is similar to that found in systems with a *broad* particle size distribution (relative to the strength of the interactions), a typical form of "uncontrolled" heterogeneity.[35,58] Note that metallic NP systems allow for greater heterogeneity while preserving collective behavior due to the presence of strong non-dipolar interactions.[59,60] Thus, in the present study the control of the heterogeneity via the proportion of LA/HA has permitted to isolate the influence of this parameter from that of local anisotropy: e.g., M2-100 shows a smaller memory effect than M2-0 due to the much larger anisotropy of the NPs in the former sample, but the negligible memory in M2-50 (with a smaller average NP anisotropy than M2-100) must be then caused by the heterogeneity obtained by mixing the two types of particles.

Next, we examine the high-field behavior (hysteresis loops) of the two series. As can be seen in Figure 4, the end members of the M1 series have rather similar saturation magnetization, M_S (although different magnetic moment, $\mu = M_S \cdot V$) and coercivity, H_C. On the other hand, the Co-doped NPs have a smaller M_S than the pure maghemite NPs, but a much larger H_C. The smaller M_S is probably due to increased disorder, presumably at the surface, as indicated by the observation of exchange bias (field-axis shift of the low temperature loop after cooling in a saturating field[61]).[62–64] Interestingly, in contrast with the qualitatively similar trends of the ZFC curves for the two series, the hysteresis loops of the two types of mixtures are very different (Figure 4). While the M1 samples present ordinary (single-phase-like) loops, the M2 mixtures display double-loop responses. Such constricted loops are typical of weakly dipolar-coupled composites,[14] strongly exchange-coupled systems with exceedingly large soft counterparts (e.g., in polycrystalline bulk materials, thin films or core/shell nanoparticles),[65–67] weakly exchange-coupled composites (in different morphologies)[65–67] or poorly-mixed (or phase-segregated) systems.[20,40] This was expected from the fact that the average dipole-dipole interaction strength in the M2-50 sample amounts to a field of ~140 Oe (after equating dipolar and Zeeman energies using the NP magnetic moments obtained as indicated in Figure S3), significantly lower than the difference in coercivity between the constituent particles (see Figure 4). In contrast, for M1-50 the corresponding average *dipolar field* is ~220 Oe, *i.e.*, larger than the coercivity difference between the LA and HA particles in series M1.

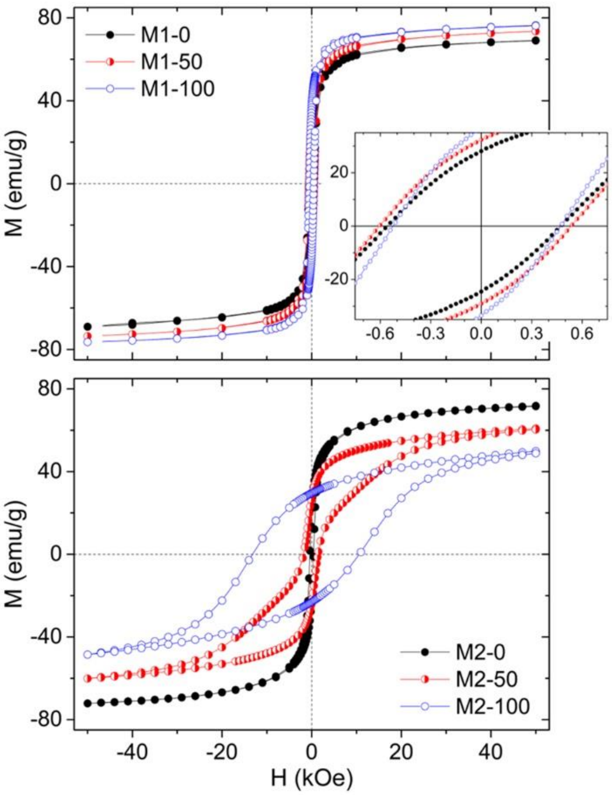

Figure 4. Hysteresis loops at 5 K after field cooling measured for the end and middle members of each sample series. The inset in the upper panel shows the low-field, hysteretic region.

Notably, although the overall shape of the measured loops is reasonably well-described as a superposition of the end member loops (see Figure 5), significant deviations appear at low fields for the central samples (see insets), yielding field-axis interception values larger than those extracted from the calculated superpositions. This result is, in fact, in agreement with the naïve picture of the harder particles providing some "pinning" against the switching of the softer particles, which essentially determine the overall H_C. Thus, one would intuitively argue that the difference in anisotropy between the hard and soft particles is high enough to prevent the full coupling of the two populations in the mixtures. However, the difference between the calculated and experimental coercivities indicate that the two types of NPs must influence each other through dipolar interactions. Thus, the soft/hard NP populations are strongly interacting (given the NPs proximity) but not fully-coupled due to the large anisotropy of the HA particles. Hence, our results highlight the ambiguity of the usual interpretation of the magnetic properties of a magnetic composite as "coupled" or "weakly coupled". To obtain the complete picture of the magnetic response, information on the field and temperature ranges should be discussed, as illustrated by the central samples in the M2 series, which show collective ("coupled") behavior at low fields and T ~ 200 K (*i.e.*, a single peak in the ZFC curve), but weak coupling at higher fields and T = 5 K (*i.e.*, separate, yet not independent, magnetization reversal of the two populations resulting in double-loop hysteresis).

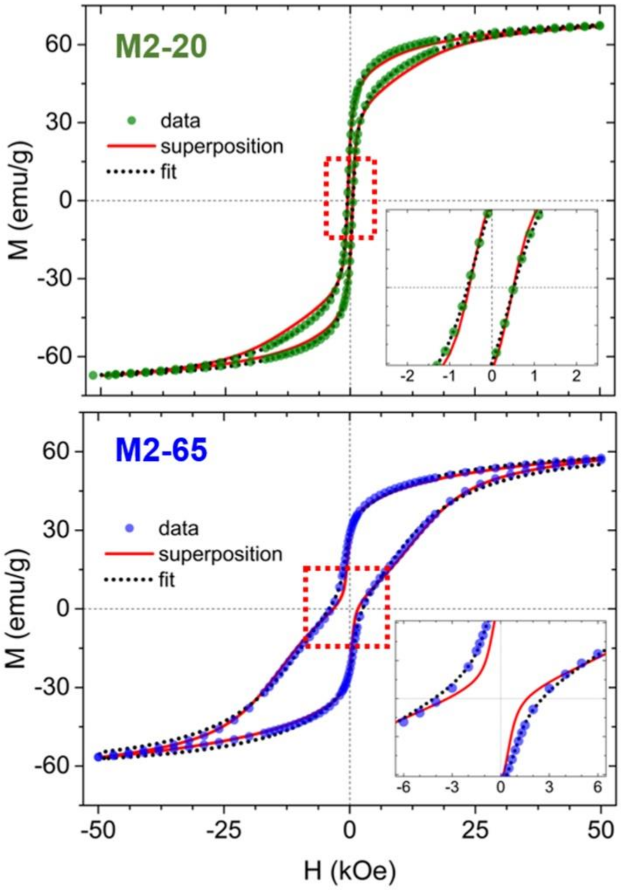

Figure 5. Hysteresis loops at 5 K after field cooling measured for two selected samples in the M2 series. The insets zoom the central region. The red line is the weighted superposition of the end members of the series (M2-0 and M2-100), whereas the black dotted line is the fit to a model with two interacting components (see text for details).

In the following we discuss in more detail the evolution of T_{MAX} and H_C on the proportion of HA particles, *x*, in the two series studied, as summarized in the two left columns in Figure 6. Firstly, we examine the data measured (or calculated) in the M1 series, *i.e.*, the left column in Figure 6. The freezing temperature (T_{MAX}) shows a clear linear trend, which can be understood by assuming that the individual blocking temperatures have no bearing on the collective freezing, *i.e.*, they are fully determined by the strong interparticle interactions, as first proposed by Mørup in the 90's[68] and suggested by the high T_{MAX}/T_B ratio for the end members of the series. The data in the M1 series is well described by this model, where T_{MAX} is proportional to the dipolar interaction strength between nearest neighbors T_{dd},[39,68]

$$T_{MAX} \propto T_{dd} \propto \frac{\mu_{av}^2}{r^3} \propto M_S C \mu_{av} = M_S C[\mu_{LA} + (\mu_{HA} - \mu_{LA})x] \tag{1}$$

where μ_{av} is the weighted average magnetic moment of the high- (μ_{HA}) and low- (μ_{LA}) anisotropy particles, and C is the NP packing fraction/filling factor. Note that C and M_S are roughly constant across the series. A constant $C \approx 60\%$ results from the fact that all samples have been compacted under the same pressure, yielding quasi-random-close-packed configurations,[50] as shown in Figure 1(c). Given the modest difference in diameter between the small (LA) and large (HA) particles (1.28 ratio), the filling factor will barely change with the fraction of HA particles.[69] The saturation magnetization of the large particles was measured to be only slightly larger than that of the small particles, as seen in Figure 4 upper panel.[45] Therefore, dipolar interactions depend on x mainly through the volume-averaged particle moment, μ_{av}, which varies linearly from the moment of the small particles to that of the large particles (μ_{LA} and μ_{HA}, respectively). Thus, the experimental observation of a linear dependence of T_{MAX} on x is consistent with a model where the ZFC peak temperature is determined exclusively by the relatively strong dipolar interparticle interactions.

In these strongly coupled M1 mixtures, while T_{MAX} is solely determined by interactions, H_C is shown to be determined both by the intrinsic value in isolated NPs and by the intensity of the interparticle interactions. The H_C values measured across the series deviate from the values extracted from the superposition loops, indicating an influence of the varying interaction strength. In fact, the observed non-monotonic dependence can be explained by a simple model which considers the variation across the series of both the average particle size and the interparticle interactions. The H_C of a dense NP assembly results from two factors, the individual particle anisotropy barrier and the strength of interparticle interactions, which may be quantified by T_{dd} (Equation 1). Regarding the first factor, it is well-known that the coercivity is proportional to the anisotropy barrier ($\propto$ KV),[70] which, in turn (and given the similar K values previously measured for the particles in M1-0 and M1-100)[45] depends linearly on *x*. Thus, the *isolated-particle coercivity* of the average particle in the composite M1-*x* can be written as

$$H_{C,ip}(x) = H_{C,LA} + \left(H_{C,HA} - H_{C,LA}\right)x \qquad (2)$$

where $H_{C,LA}$ and $H_{C,HA}$ are the coercive fields of the small and large particles, respectively. Regarding the effect of dipolar interactions, experiments dealing with differently concentrated dispersions of particles have established a decrease of H_C with increasing particle concentration at temperatures well below the blocking temperature.[71] This is in agreement with the classical calculations by Néel[72] and Wohlfarth,[73] as well as with numerical simulations, which found a linear dependence between the two parameteres.[74] With $T_{dd} \propto C\mu_{av}$ for the strength of dipolar interactions in the M1 series, the present experiment is complementary to the cited previous experiments, as here the "concentration" *C* (packing fraction) is constant and the average particle moment is finely tuned *via* the HA/LA proportion. Thus, the H_C of the sample M1-*x* can be written as

$$H_C(x) = H_{C,ip}(x)[1 - AT_{dd}(x)] \qquad (3)$$

inserting T_{dd} from Equation 1 yields

$$H_C(x) \propto \{H_{C,LA} + (H_{C,HA} - H_{C,LA})x\} * \{1 - B[\mu_{LA} + (\mu_{HA} - \mu_{LA})x]\} \qquad (4)$$

where A and B are constants. This is an inverted parabola, as experimentally observed in series M1 [see Figure 6(b1)], which supports the mentioned approximations and hypotheses leading to Equation 4. Hence, intermediate compositions show a stronger effect of interactions (even if they increase monotonically in the series) and the coercivity of the uniform mixtures deviate more from the simple superposition of the two NP populations.

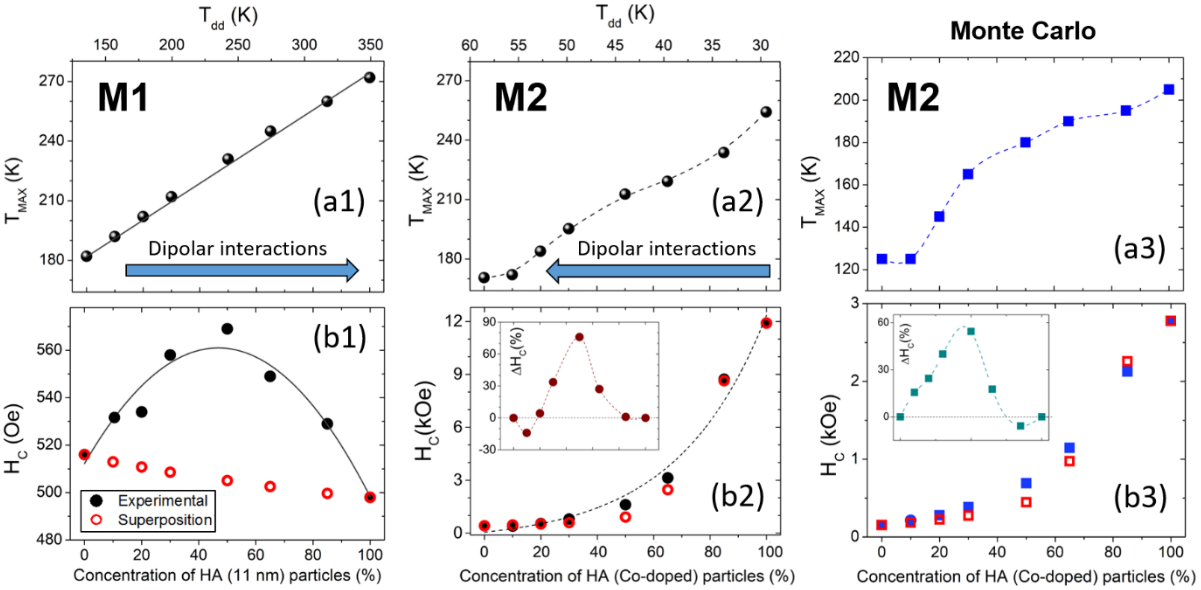

Figure 6. Dependence on the concentration of high anisotropy particles of the ZFC peak temperature, T_{MAX} (a), and the coercivity, H_C (b). The third column shows the results from Monte Carlo simulations for the M2 series. The empty red symbols in panels (b) correspond to values extracted from loops calculated as (weighted) superpositions of the loops measured (or simulated) for the end members of the series. The insets plot the relative difference between the values measured (or extracted from simulations) in the mixtures and in the superposition loops. The solid lines in the first column are fits to the models

described in the text, while the dotted lines are guides to the eye. Note that the upper x-axes give the variation of the dipolar interaction strength, T_{dd}, as a result of the different magnetic moments of the LA and HA constituent particles. The arrows in (a1) and (a2) highlight the fact that while T_{dd} increases with x in the M1 series it decreases in the M2 series.

Next, we discuss the same magnetic parameters in the M2 series, plotted in the central column of Figure 6, and compare them to those in the M1 series. The dependence of T_{MAX} on x for the M2 series appears similar (increasing trend) to that of the M1 series. However, there is a crucial difference, highlighted by the upper axes in Figure 6(a1) and (a2), showing the variation of the average dipole-dipole interaction strength T_{dd} with the mix proportion; namely, while T_{dd} increases with x in the M1 series, it decreases in the M2 series. This is because the magnetic moment of the Co-doped (HA) particles is smaller than that of the pure maghemite (LA) particles (see Figure S3 in the SI), thus T_{dd} decreases (concomitantly with the increase in average local anisotropy) as the proportion of the lower-moment HA particles, x, becomes larger. Consequently, this rules out dipolar interactions as the origin of the increase in T_{MAX} with x and points out the significant influence of the local anisotropy on this characteristic temperature. Importantly, the data does not imply that dipolar interactions, although less intense than in series M1, are not also influencing the value of T_{MAX}. In fact, the existence of a single peak at this temperature can only be understood from the presence of strong enough interactions. Nevertheless, the average local anisotropy energy is larger and varies much faster across the series than the intensity of dipolar interactions, the ratio between the two energy terms (KV/E_{dd} =

$25T_B/T_{dd}$) ranging from roughly 7 (for M2-0) to about 120 (in M2-100). Mørup's model, which was found to describe well the variation of T_{MAX} in series M1, cannot account for $T_{MAX}(x)$ in the M2 series. Note that the dipolar coupling strength does not necessarily have to trump the anisotropy barrier in order to yield (low-field) collective behavior. For instance, sample M2-100, with an E_{dd}/KV ratio of barely 1%, does show clear-cut superspin glass features such as ZFC memory [see Figure 3(d)] and critical slowing down of the relaxation time (not shown). This might be attributed to the narrow size (KV) distribution and a mechanism whereby the random orientation of the NP easy axes contributes to the energy degeneracy characteristic of frustrated behavior and allows the appearance of superspin glass behavior despite the relatively weak dipolar coupling, as suggested in a recent Monte Carlo study by J. J. Alonso *et al.*[75]

Regarding the coercive field, the experimental H_C values also lie above the superposition values (panel b2 in Figure 6), as in the M1 series, but the enhancement due to uniform mixing is much larger (up to 80% for M2-50, see inset). This indicates that despite the double-loop behavior (signaling that the two populations are not fully coupled), the strong interaction between the particles significantly influence their magnetism. However, as discussed above, increasing concentrations of HA particles in this series provide *weaker* average dipolar interactions, therefore the model applied above for the M1 series is completely inadequate in the (relatively) weakly coupled M2 scenario, where the simpler intuitive idea of the harder particles "pinning" the switching of the softer ones, which in turn determine the overall coercivity, appears more suitable. Note that a minimum population of around 20% of HA particles is necessary for the soft particles to *feel* such pinning influence. The contrast between the two series in the influence of dipolar interactions on H_C is thus remarkable.

The third column in Figure 6 shows results from Monte Carlo simulations of the M2 series. The concentration dependence of the parameters extracted from the simulated thermal and magnetic response (see SI for representative examples, Figures S5 and S6) are remarkably similar to the experimental observations, including the effect on the coercivity of mixing *versus* simple (unmixed) addition of the soft and hard nanoparticles [insets in panels (b2) and (b3)]. The relatively simpler, strongly coupled, M1 series was also simulated, with results again very similar to the experiment (see SI, Figure S4).

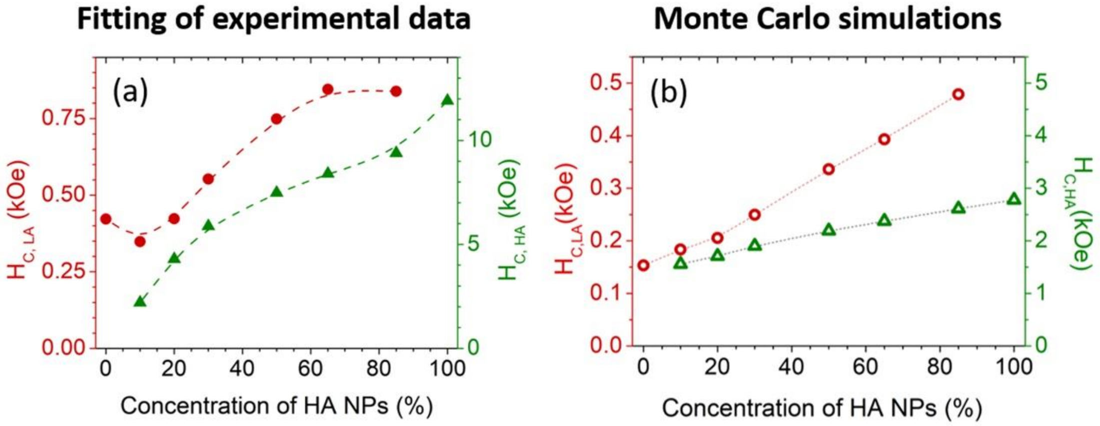

Figure 7. Coercive fields of the LA/HA NP populations as extracted from the fitting of experimental loops (a) and Monte Carlo-simulated loops (b) as a function of hard (Co-doped) particles concentration.

In order to explore the origin of the *x* dependence of the hysteresis loops in series M2 (summarized in panel b2 of Figure 6), we have attempted to extract the behavior of each population (LA and HA particles) by fitting the experimental loops to the following sum of *hard* and *soft* components using the empirical function proposed by Stearns and Cheng:[76]

$$M(H) = \frac{2}{\pi} M_{S,LA} \operatorname{atan}\left[\left(\frac{H+ H_{E,LA} \pm H_{C,LA}}{H_{C,LA}}\right) \tan\left(\frac{\pi S_{LA}}{2}\right)\right] + \frac{2}{\pi} M_{S,HA} \operatorname{atan}\left[\left(\frac{H+ H_{E,HA} \pm H_{C,HA}}{H_{C,HA}}\right) tan\left(\frac{\pi S_{HA}}{2}\right)\right] \tag{5}$$

where the ± symbol indicates the different sign used in the simultaneous fitting of the ascending and descending branches of the loops, and the squareness parameters (S) were obtained from the fitting of the end member loops (*i.e.*, it is assumed not to change significantly when mixing the two types of NPs). Note that the exchange bias of the loops is taken into account in the fit, $H_{E,LA}$ and $H_{E,HA}$. Two examples of the fitted curves are given in Figure 5. The results for H_C as a function of the proportion of HA particles, *x*, plotted in the left panels of Figure 7, show a strong mutual influence of one type of particle on the other. Interestingly, the results are qualitatively reproduced by the Monte Carlo simulations (where it is straightforward to separate the individual contributions of the two particle populations to the total hysteresis loop). Thus, not only the hard particles *harden* the soft ones, as expected, by *delaying* their switching as commented above, but, conversely, the introduction of soft particles in a compact with majority of hard particles will *soften* them. This is the reason why the overall result of introducing hard particles in the binary compacts [increasing *x* in Figure 6(b2)] is a faster-than-linear enhancement of coercivity, as both components (LA and HA) are increasing their coercivity.

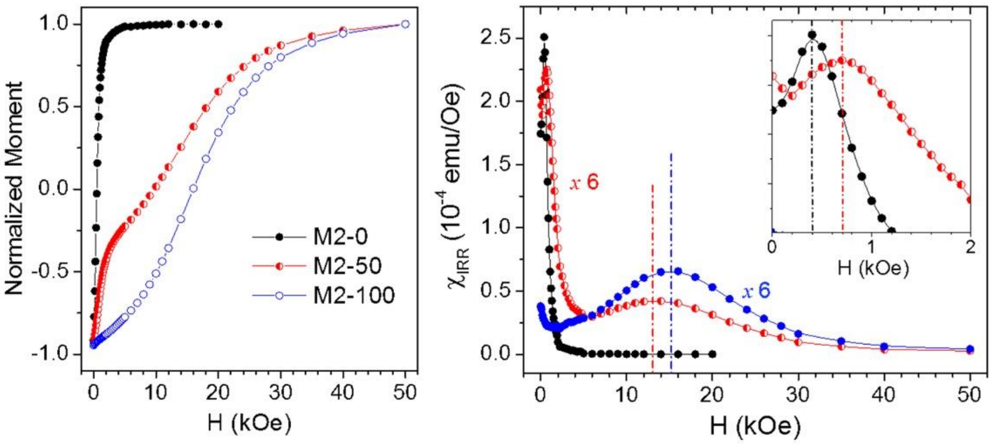

Figure 8. Switching field distributions (right panel) for the end and central members of the M2 series as obtained from the derivative of the DC demagnetization remanence (M_{DCD}) curves shown in the left panel. All curves were measured at a temperature of 5 K. The inset zooms in the low field region to show the deviation of the soft mode in the M2-50 mixture from the single peak observed in the M2-0 compact.

The relatively weak, but still significant, soft-hard particle coupling can be conveniently quantified by the analysis of the switching field distribution, defined as the field necessary to overcome the energy barrier during an irreversible reversal process (and therefore offering a measure of such anisotropy barrier distribution), which can be extracted from the dc demagnetization remanence (M_{DCD}) curve as $\chi_{irr} = dM_{DCD}/dH$.[40,77] Figure 8 shows the M_{DCD} curves and corresponding switching field distributions for the end and central members of the M2 series. As expected from the overall aspect of its hysteresis loop, the central sample of the series, M2-50, shows two well-separated switching modes, soft (at low fields) and hard, which justifies the description of this composite as "weakly coupled". However, those modes are clearly shifted towards each other with respect to the switching behavior of the *pure* compacts M2-0 and M2-100, in agreement with the results from the Monte Carlo and fitting analyses above. It is this mutual influence that explains that the coercive field measured for sample M2-50 are considerably different from those of an unmixed system with the same components (see Figure 6, panels b2 and b3).

Therefore, despite the double-loop behavior of the hysteresis loop, Figure 7 and 8 clearly indicate that dipolar interactions between the HA and LA particles significantly affect their individual switching, suggesting the labels *modified single-particle response* or *weak coupling* to describe their behavior. The coupling, however, is high enough to render a single peak in the ZFC curve of the mixtures [see Figure 3(b)].

Altogether the results draw a complex scenario for the M2 mixtures, which present both seemingly “collective” (T_{MAX}) and “single-particle” (H_C) properties. In fact, the only “collective” property observed in these mixtures is the blocking temperature, although its increase with decreasing interactions and increasing local anisotropy already signals a dominant role for the latter factor. On the other hand, (i) the constricted hysteresis loops, (ii) the lack of ZFC *memory*, and (iii) the hump of the M(T) at low temperatures, they all correspond to a “two-phase” behavior driven by the large anisotropy contrast between the LA and HA particles.

The origin of the distinct difference between the M1 and M2 series must lie on the large anisotropy of the Co-doped maghemite nanoparticles. Based on the Random Anisotropy Model (RAM), in nanocrystalline materials the structural correlated volume, (*i.e.*, nanoparticle size) can actually be smaller than the volume of magnetically correlated material due to the coupling among particles/grains. Hence, within this framework, the magnetization reversal of such magnetic correlated volume is not ruled by the intrinsic properties of the individual particles, but by an effective "averaged" anisotropy and easy axis resulting from the scaling of the individual contribution of each particle/grain randomly oriented within the "magnetic cluster" (i.e., the magnetically correlated volume).[78–81] For bulk nanocrystalline materials (*i.e.*, with exchange interacting grains), the region which influences the magnetization is given by the ferromagnetic correlation length, $L_{corr} = \sqrt{A_{ex}/K}$ (where K is the anisotropy constant and A_{ex} is the exchange stiffness, which can be naïvely considered as the "force" trying to keep the spins parallel to each other). However, the RAM approach has been proposed to be independent of the source of the magnetic coupling and it should be appropriate for other types of interactions, like dipolar interactions.[79] Indeed, recent experimental observations have shown a good agreement with this model for ensemble of particles interacting purely by dipolar coupling.[82,83] However, for purely dipolar interacting systems, A_{ex} is not the adequate parameter to define the tendency of neighboring magnetic moments to be correlated due to dipolar interactions. Thus, A_{ex} can be qualitatively substituted by an "effective dipolar coupling stiffness", A_{dip}. Namely, A_{dip} can be understood as the "strength" of the effective dipolar interaction among the particles.[79,82] However, note that this quantity should be considered as the coupling strength of the weakest interactions and not as an average value of the coupling.[79] Therefore, a (dipolar) correlation length can be estimated as $L_{corr} = \sqrt{A_{dip}/K}$. This L_{corr} can be interpreted as the average distance over which the magnetization fluctuations are correlated. Thus, materials with a weak anisotropy, like γ-Fe_2O_3, should have a large L_{corr}, but Co-ferrite, with a large K, should have a small L_{corr}.

In fact, information on the intensity of the interparticle interactions can be extracted from the field dependence of T_B. Namely, using the well-known $T_B(H)$ for nanoparticles, $T_B = \frac{KV}{k_B \ln\left(\frac{\tau_m}{\tau_0}\right)}\left[1 - \frac{\mu_0 H}{\mu_0 H_K}\right]^{1.5}$, but taking into account the correlated volume (rather than the nanoparticle volume) and the effective, scaled, anisotropy of this correlated volume (rather than the intrinsic anisotropy of the nanoparticles); i.e., $V_N = \frac{\pi}{6}[D^3 + x(L_{corr}^3 - D^3)]$ (with D the particle diameter and *x* the packing fraction), and $K_{eff} = \frac{K}{\sqrt{N}}$ (with *N* the number of particles contained in V_N), respectively.[81] See the SI for a more detailed derivation.[84,85]

By fitting the experimental $T_B(H)$ for the two pure cases of the M2 series, *i.e.*, M2-0 and M2-100 (see Figure S7) we obtain that, certainly, L_{corr} for the γ-Fe_2O_3 is considerably larger than that obtained for the Co-doped γ-Fe_2O_3 particles (Table 1). In fact, $L_{corr}(\gamma\text{-}Fe_2O_3)$ = 36(1) nm encloses tens of nanoparticles (with D ≈ 6.8 nm) thus the magnetic properties of the pure maghemite particles in M2-0 are averaged over many particles. On the other hand, L_{corr}(Co-doped) = 11.4(5) corresponds to a correlated volume comprising barely 4 particles; consequently, the properties of the dense system made of Co-doped particles should be more individual-particle-like than those of M2-0, as observed experimentally.

Table 1. Correlation length (L_{corr}) for different samples of the M2 series obtained from the fit to a dipolar random-anisotropy model.

Sample	L_{corr} (nm)
M2-0	36(1)
M2-10	13.2(5)

M2-50	11.2(5)
M2-85	10.8(5)
M2-100	11.4(5)

Notably, the RAM approach described above has been developed for homogeneous mixtures of particles.[82,86] However, assuming that the approach holds even for binary mixtures, we can estimate the "average" L_{corr} from the $T_B(H)$. Remarkably, the values obtained for the binary mixtures show that even a 10% of hard nanoparticles in the mixture is sufficient to reduce L_{corr} to the M2-100 level.

We have thus demonstrated the fabrication of uniform binary compacts mixing nanoparticles with different magnetic anisotropy. The large density, or filling factor (≈ 60%),[50] achieved by simply pressing a powder of *bare* nanoparticles makes the resultant pellets promising candidates to build novel nanoparticulated magnetic ceramics after a mild sintering stage preserving the individual particle morphology, thus creating the disordered analogues of the recently reported bulk *supercrystals* densified by controlled annealing or ligand-exchange.[5,87] In other words, to build dense "superglasses", whose overall behavior may be finely tailored *via* the added degrees of freedom of the proportion and properties of the individual components in binary systems; here, such control has been shown to go beyond the superposition of uncoupled systems (as exemplified, e.g., by the strong increase in low temperature coercivity in the central samples of series M2). For magnetic materials, this strategy may prove useful for the design of, e.g., composites with magnetically-enhanced mechanical stability[11] or permanent magnets with optimized energy product.[19,20]

The latter necessarily involve exchange coupling between the constituent nanoparticles, which has been recently shown to be achievable while preserving the individual character and even the shape of the particles by using advanced densification techniques.[14,88] In this context, an advantage of magnetic binary systems is that loop constrictions (like those in Figure 5) could be exploited as a sensitive indicator of the lack of significant interparticle exchange to monitor such densification processes,[14] as we intend to demonstrate in future studies.

CONCLUSIONS

We have shown the convenience of dense hard/soft binary nanoparticle assemblies to discern the single-particle/collective nature of different properties in a given system. The influence of dipolar interactions, (average) local anisotropy, and sample heterogeneity on the low-field (blocking temperature, relaxation) and high-field (hysteresis loop) magnetic response has been illustrated in two series of strongly interacting, but strongly- (M1 series) and weakly-coupled (M2 series) composites resulting from different anisotropy ratios of the mixed hard/soft NP constituents.

The ZFC peak temperature (T_{MAX}) is a collective property in all samples studied. However, whereas in the M1 series T_{MAX} is entirely determined by interparticle interactions, the M2 series presents a more complex scenario where the average local anisotropy provides a growing contribution with increasing concentration of the high anisotropy Co-doped NPs. Thus, the strong increase of the average anisotropy across this series (a factor of 8.2) overcomes the smaller reduction in dipolar energy (factor of ~1.6) to account for the observed increase in T_{MAX}. Nonetheless, it is the presence of strong interparticle interactions that enable, in the first place, the local averaging of anisotropy to yield a single stabilization temperature at T_{MAX}. However, in contrast with the M1 series, in the M2 mixtures the slow relaxation of the NPs moments below this temperature does not exhibit the ZFC memory effect characteristic of the (collective) superspin glass state, indicating a lack of homogeneous (single-phase) relaxation of the magnetization. More importantly, we have demonstrated the fundamentally different effect that dipolar interactions can have in nanoparticle composites depending on the anisotropy difference between the constituent NP populations. We have shown how binary random compacts with sufficiently high anisotropy contrast (*i.e.*, the M2 series) may be employed as a tool to test or, rather, define the *collective* character of a given magnetic property as that resulting in the collapse of the individual features caused by strong enough interactions. Crucially, such collective character must, in general, be ascribed to specific properties and not to the system as a whole.

METHODS

Samples preparation. Four types of highly uniform, roughly spherical NPs were synthesized using an optimized thermal decomposition route[64]: maghemite NPs with average diameters d_{TEM} = 6.8, 9.0 and 11.5 nm, and cobalt-doped (Co:Fe = 0.19:1) maghemite particles 6.8 nm in diameter (see Figure 1). Iron pentacarbonyl [$Fe(CO)_5$] was thermally decomposed in the presence of oleic acid (surfactant) and dioctyl ether (solvent), and subsequently oxidized with trimethylamine N-oxide [$(CH_3)_3NO$] at high temperature. The nanoparticle size was controlled changing the amount of oleic acid in the reaction, e.g.

for the 6.8, 9.0 and 11.5 nm particles, 1.7, 2.3 and 3.0 mol equivalents of oleic acid were used, respectively.[64] The Co-doped maghemite nanoparticles were prepared by simply replacing the corresponding fraction of $Fe(CO)_5$ by $Co(CO)_5$ to yield the above-mentioned Co:Fe ratio, which has been previously shown to produce a large increase in NP anisotropy while reducing only slightly the saturation magnetization.[46] The 9.0 and 11.5 nm NPs (corresponding to a volume ratio of 2), and the equally-sized, 6.8 nm, pure and Co-doped maghemite NPs, were mixed in different proportions while still in liquid solution to prepare the samples in series M1 and M2, respectively. The mixed solutions of nanoparticles were washed repeatedly in acetone to remove the oleic acid coating. Thermogravimetry analysis shows that an organic residue of only ≈ 5%w still remains bound to the NPs. The suspension was dried and the resulting powder compacted uniaxially under ≈ 1 GPa to yield dense discs with about 60% in filling factor, as estimated using a method based on the analysis of demagnetizing field effects recently developed by some of us.[50]

Magnetic characterization. The hysteresis loops were measured at 5 K after cooling in a 50 kOe field, which was also the maximum field used in the loops. The temperature dependence of the magnetization, M(T), (in a field H = 5 Oe in the disk plane) after field-cooling (FC) and zero-field cooling (ZFC) was also registered. In addition, *memory* ZFC curves were also measured. Namely, the cooling was halted during 4 hours at a given temperature, T_{halt}, below the ZFC peak temperature T_{MAX} ($T_{halt} \sim 2 \cdot T_{MAX}/3$), then resumed to the lowest temperature (10 K). Subsequently, the M(T) curve is registered under exactly the same conditions as the reference ZFC curve. DCD (direct current demagnetization) remanence curves were measured by initially saturating the sample (in H = -50 kOe) and then measuring the moment after application and removal of progressively increasing reverse fields.[89] Finally, the temperature dependence of the ac susceptibility was recorded at 10 Hz using a field amplitude of 1 Oe. All the magnetic measurements were performed using a MPMS SQUID magnetometer from Quantum Design. Note that, although the studied dense disks present a substantial shape anisotropy, demagnetizing field corrections were not necessary, as we have previously demonstrated that such corrections sharpen the ZFC peak but do *not* shift its position (T_B, the relevant low-field parameter in this work).[50]

Monte Carlo simulations. Monte Carlo simulations were carried out using the mesoscopic three-spins model,[57] with parameters extracted from bulk values and experimental results (see SI for details). [46,57,90–102]

ASSOCIATED CONTENT

Supporting Information Available: Extended magnetic experimental and theoretical data. Monte Carlo simulation model and random anisotropy model (RAM). This material is available free of charge via the Internet at http://pubs.acs.org.

AUTHOR INFORMATION

Corresponding Authors

* E-mail: joseangel.toro@uclm.es

* E-mail: josep.nogues@icn2.cat

* E-mail: elena.hsanchez@uclm.es

ORCID ID

Jose A. De Toro: 0000-0002-9075-1697

Josep Nogués: 0000-0003-4616-1371

Elena H. Sánchez: 0000-0001-5737-0035

AUTHORS CONTRIBUTIONS

J.A.T designed the experiment, J.N. expanded it to series M2; both coordinated the data analysis and discussion. S.S.L synthesized the nanoparticles and characterized them by TEM. E.H.S. and P.S.N. prepared the compacts, measured and analysed the M(T) and M(H) data. R.M, M.S.A and P.N are responsible for the memory measurements and their analysis. M.V and K.N.T performed the Monte Carlo simulations. M.M. and P.C.R contributed to the magnetic characterization and performed the fittings of the two-phase hysteresis loops. G.S. analysed the mixtures homogeneity by SEM/EDS. G.M. and D.P. performed the RAM analysis. All authors contributed to the results discussion and revision of the article, which was written mainly by J.A.T., J.N. and E.H.S.

ACKNOWLEDGMENTS

This work was supported by the Spanish Ministerio de Economía y Competitividad (grants MAT2015-65295-R and MAT2016-77391-R). JN also acknowledges funding from the Generalitat de Catalunya through the 2017-SGR-292 grant. ICN2 is funded by the CERCA Programme / Generalitat de Catalunya. The ICN2 is supported by the Severo Ochoa Centers of Excellence program, funded by the Spanish Research Agency (AEI, grant no. SEV-2017-0706). MSA, RM and PN acknowledge support from The Swedish Research Council (VR). The UCLM authors acknowledge technical help from Mario Rivera and Eduardo Prado.

REFERENCES

(1) Deng, Y.; Ediriwickrema, A.; Yang, F.; Lewis, J.; Girardi, M.; Saltzman, W. M. A Sunblock Based on Bioadhesive Nanoparticles. *Nat. Mater.* **2015**, *14*, 1278–1285.

(2) Jordan, A.; Maier-Hauff, K.; Wust, P.; Rau, B.; Johannsen, M. Thermotherapie Mit Magnetischen Nanopartikeln. *Onkologe* **2007**, *13*, 894–902.

(3) Salata, O. V. Applications of Nanoparticles in Biology and Medicine. *J. Nanobiotechnol.* **2004**, *2*, 3.

(4) Cabrera, D.; Coene, A.; Leliaert, J.; Arte, E. J.; Dupre, L.; Telling, N. D.; Teran, F. J. Dynamical Magnetic Response of Iron Oxide Nanoparticles Inside Live Cells. *ACS Nano* **2018**, *12*, 2741–2752.

(5) Dreyer, A.; Feld, A.; Kornowski, A.; Yilmaz, E. D.; Noei, H.; Meyer, A.; Krekeler, T.; Jiao, C.; Stierle, A.; Abetz, V.; Weller, H.; Schneider, G. A. Organically Linked Iron Oxide Nanoparticle Supercrystals with Exceptional Isotropic Mechanical Properties. *Nat. Mater.* **2016**, *15*, 522–528.

(6) Wang, T.; Zhuang, J.; Lynch, J.; Chen, O.; Wang, Z.; Wang, X.; LaMontagne, D.; Wu, H.; Wang, Z.; Cao, Y. C. Self-Assembled Colloidal Superparticles from Nanorods. *Science* **2012**, *338*, 358–363.

(7) Weidman, M. C.; Smilgies, D. M.; Tisdale, W. A. Kinetics of the Self-Assembly of Nanocrystal Superlattices Measured by Real-Time in Situ X-Ray Scattering. *Nat. Mater.* **2016**, *15*, 775–781.

(8) Farrell, D. F.; Ijiri, Y.; Kelly, C. V; Borchers, J. A.; Rhyne, J. J.; Ding, Y.; Majetich, S. A. Small Angle Neutron Scattering Study of Disordered and Crystalline Iron Nanoparticle Assemblies. *J. Magn. Magn. Mater.* **2006**, *303*, 318–322.

(9) Lisiecki, I.; Parker, D.; Salzemann, C.; Pileni, M. P. Face-Centered Cubic Supra-Crystals and Disordered Three-Dimensional Assemblies of 7.5 nm Cobalt Nanocrystals: Influence of the Mesoscopic Ordering on the Magnetic Properties. *Chem. Mater.* **2007**, *19*, 4030–4036.

(10) Singh, G.; Chan, H.; Baskin, A.; Gelman, E.; Repnin, N.; Kral, P.; Klajn, R. Self-Assembly of Magnetite Nanocubes into Helical Superstructures. *Science* **2014**, *345*, 1149–1153.

(11) Håkonsen, V.; Singh, G.; Normile, P. S.; De Toro, J. A.; Wahlström, E.; He, J.; Zhang, Z. Magnetically Enhanced Mechanical Stability and Super-Size Effects in Self-Assembled Superstructures of Nanocubes. *Adv. Funct. Mater.* **2019**, *29*, 1904825.

(12) Shevchenko, E. V.; Talapin, D. V.; Kotov, N. A.; O'Brien, S.; Murray, C. B. Structural Diversity in Binary Nanoparticle Superlattices. *Nature* **2006**, *439*, 55–59.

(13) Yang, Z.; Wei, J.; Bonville, P.; Pileni, M. P. Engineering the Magnetic Dipolar Interactions in 3D Binary Supracrystals *via* Mesoscale Alloying. *Adv. Funct. Mater.* **2015**, *25*, 4908–4915.

(14) Chen, J.; Ye, X.; Oh, S. J.; Kikkawa, J. M.; Kagan, C. R.; Murray, C. B. Bistable Magnetoresistance Switching in Exchange-Coupled $CoFe_2O_4$-Fe_3O_4 Binary

Nanocrystal Superlattices by Self-Assembly and Thermal Annealing. *ACS Nano* **2013**, *7*, 1478–1486.

(15) Chen, J.; Dong, A.; Cai, J.; Ye, X.; Kang, Y.; Kikkawa, J. M.; Murray, C. B. Collective Dipolar Interactions in Self-Assembled Magnetic Binary Nanocrystal Superlattice Membranes. *Nano Lett.* **2010**, *10*, 5103–5108.

(16) Balasubramanian, B.; Das, B.; Skomski, R.; Zhang, W. Y.; Sellmyer, D. J. Novel Nanostructured Rare-Earth-Free Magnetic Materials with High Energy Products. *Adv. Mater.* **2013**, *25*, 6090–6093.

(17) Kneller, E. F.; Hawig, R. The Exchange-Spring Magnet: A New Material Principle for Permanent Magnets. *IEEE Trans. Magn.* **1991**, *27*, 3588–3600.

(18) Thiele, J.-U.; Maat, S.; Fullerton, E. E. FeRh/FePt Exchange Spring Films for Thermally Assisted Magnetic Recording Media. *Appl. Phys. Lett.* **2003**, *82*, 2859–2861.

(19) Jiang, J. S.; Bader, S. D. Rational Design of the Exchange-Spring Permanent Magnet. *J. Phys.: Condens. Matter* **2014**, *26*, 064214.

(20) Zeng, H.; Li, J.; Liu, J. P.; Wang, Z. L.; Sun, S. Exchange-Coupled Nanocomposite Magnets by Nanoparticle Self-Assembly. *Nature* **2002**, *420*, 395–398.

(21) Liu, X.; He, S.; Qiu, J.-M.; Wang, J.-P. Nanocomposite Exchange-Spring Magnet Synthesized by Gas Phase Method: From Isotropic to Anisotropic. *Appl. Phys. Lett.* **2011**, *98*, 222507.

(22) De Toro, J. A.; Lee, S. S.; Salazar, D.; Cheong, J. L.; Normile, P. S.; Muñiz, P.; Riveiro, J. M.; Hillenkamp, M.; Tournus, F.; Tamion, A.; Nordblad, P. A Nanoparticle Replica of the Spin-Glass State. *Appl. Phys. Lett.* **2013**, *102*, 183104.

(23) De Toro, J. A.; Normile, P. S.; Lee, S. S.; Salazar, D.; Cheong, J. L.; Muñiz, P.; Riveiro, J. M.; Hillenkamp, M.; Tournus, F.; Tamion, A.; Nordblad, P. Controlled Close-Packing of Ferrimagnetic Nanoparticles: An Assessment of the Role of Interparticle Superexchange *versus* Dipolar Interactions. *J. Phys. Chem. C* **2013**, *117*, 10213–10219.

(24) Nordblad, P. Competing Interaction in Magnets: The Root of Ordered Disorder or Only Frustration? *Phys. Scr.* **2013**, *88*, 058301.

(25) Djurberg, C.; Svedlindh, P.; Nordblad, P. Dynamics of an Interacting Particle System : Evidence of Critical Slowing Down. *Phys. Rev. Lett.* **1997**, *79*, 5154–5157.

(26) Gavilán, H.; Sánchez, E. H.; Brollo, M. E. F.; Asín, L.; Moerner, K. K.; Frandsen, C.; Lázaro, F. J.; Serna, C. J.; Veintemillas-Verdaguer, S.; Morales, M. P.; Gutiérrez, L. Formation Mechanism of Maghemite Nanoflowers Synthesized by a Polyol-Mediated Process. *ACS Omega* **2017**, *2*, 7172–7184.

(27) Hayashi, K.; Nakamura, M.; Sakamoto, W.; Yogo, T.; Miki, H.; Ozaki, S.; Abe, M.; Matsumoto, T.; Ishimura, K. Superparamagnetic Nanoparticle Clusters for Cancer Theranostics Combining Magnetic Resonance Imaging and Hyperthermia Treatment. *Theranostics* **2013**, *3*, 366–376.

(28) Liu, X.; Kent, N.; Ceballos, A.; Streubel, R.; Jiang, Y.; Chai, Y.; Kim, P. Y.; Forth,

J.; Hellman, F.; Shi, S.; Wang, D.; Helms, B. A.; Ashby, P. D.; Fischer, P.; Russell, T. P. Reconfigurable Ferromagnetic Liquid Droplets. *Science* **2019**, *365*, 264–267.

(29) Zhou, B. H.; Rinehart, J. D. A Size Threshold for Enhanced Magnetoresistance in Colloidally Prepared $CoFe_2O_4$ Nanoparticle Solids. *ACS Cent. Sci.* **2018**, *4*, 1222–1227.

(30) Kumar, N.; Khurana, G.; Gaur, A.; Kotnala, R. K. Room Temperature Low Field Magnetoresistance in $Sr_2FeMoO_6/Zn_xFe_{1-x}Fe_2O_4$ Composites. *J. Appl. Phys.* **2013**, *114*, 053902.

(31) Kiselev, V. V. *Collective Effects in Condensed Matter Physics*; De Gruyter Studies in Mathematical Physics 44, 2018.

(32) Watts, D. J.; Strogatz, S. H. Collective Dynamics of ‘Small-World’ Networks. *Nature* **1998**, *393*, 440–442.

(33) Dormann, J. L.; Fiorani, D.; Cherkaoui, R.; Tronc, E.; Lucari, F.; Orazio, F. D.; Spinu, L.; Noguès, M.; Kachkachi, H.; Jolivet, J. P. From Pure Superparamagnetism to Glass Collective State in γ-Fe_2O_3 Nanoparticle Assemblies. *J. Magn. Magn. Mater.* **1999**, *203*, 23–27.

(34) Fiorani, D.; Dormann, J. L.; Cherkaoui, R.; Tronc, E.; Lucari, F.; Orazio, F. D.; Spinu, L.; Nogues, M.; Garcia, A.; Testa, A. M. Collective Magnetic State in Nanoparticles Systems. *J. Magn. Magn. Mater.* **1999**, *197*, 143–147.

(35) Hansen, M. F.; Jönsson, P. E.; Nordblad, P.; Svedlindh, P. Critical Dynamics of an Interacting Magnetic Nanoparticle System. *J. Phys.: Condens. Matter* **2002**, *14*,

4901–4914.

(36) Sun, Y.; Salamon, M.; Garnier, K.; Averback, R. Memory Effects in an Interacting Magnetic Nanoparticle System. *Phys. Rev. Lett.* **2003**, *91*, 167206.

(37) Jonsson, T.; Nordblad, P.; Svedlindh, P. Dynamic Study of Dipole-Dipole Interaction Effects in a Magnetic Nanoparticle System. *Phys. Rev. B: Condens. Matter Mater. Phys.* **1998**, *57*, 497–504.

(38) Vernay, F.; Kachkachi, H. Single-Particle *versus* Collective Effects in Assemblies of Nanomagnets: Screening. *J. Magn. Magn. Mater.* **2020**, *in press*.

(39) Hansen, M. F.; Mørup, S. Models for the Dynamics of Interacting Magnetic Nanoparticles. *J. Magn. Magn. Mater.* **1998**, *184*, 262–274.

(40) Muscas, G.; Kumara, P. A.; Barucca, G.; Concas, G.; Varvaro, G.; Mathieu, R.; Peddis, D. Designing New Ferrite/Manganite Nanocomposites. *Nanoscale* **2016**, *8*, 2081–2089.

(41) Song, Q.; Zhang, Z. J. Controlled Synthesis and Magnetic Properties of Bimagnetic Spinel Ferrite $CoFe_2O_4$ and $MnFe_2O_4$ Nanocrystals with Core−Shell Architecture. *J. Am. Chem. Soc.* **2012**, *134*, 10182–10190.

(42) Trudel, S.; Hill, R. H. Magnetic Properties of Binary Mixtures of Metal Oxide Nanoparticles. *Polyhedron* **2007**, *26*, 1863–1870.

(43) Andersson, M. S.; Mathieu, R.; Normile, P. S.; Lee, S. S.; Singh, G.; Nordblad, P.; De Toro, J. A. Magnetic Properties of Nanoparticle Compacts with Controlled

Broadening of the Particle Size Distribution. *Phys. Rev. B: Condens. Matter Mater. Phys.* **2017**, *95*, 184431.

(44) Papaefthymiou, G. C.; Devlin, E.; Simopoulos, A.; Yi, D.; Riduan, S.; Lee, S. S.; Ying, J. Interparticle Interactions in Magnetic Core/Shell Nanoarchitectures. *Phys. Rev. B: Condens. Matter Mater. Phys.* **2009**, *80*, 024406.

(45) Andersson, M. S.; Mathieu, R.; Lee, S. S.; Normile, P. S.; Singh, G.; Nordblad, P.; Toro, J. A. De. Size-Dependent Surface Effects in Maghemite Nanoparticles and Its Impact on Interparticle Interactions in Dense Assemblies. *Nanotechnology* **2015**, *26*, 475703.

(46) Fantechi, E.; Campo, G.; Carta, D.; Corrias, A.; de Julián Fernández, C.; Gatteschi, D.; Innocenti, C.; Pineider, F.; Rugi, F.; Sangregorio, C. Exploring the Effect of Co Doping in Fine Maghemite Nanoparticles. *J. Phys. Chem. C* **2012**, *116*, 8261–8270.

(47) Bruvera, I. J.; Mendoza Zélis, P.; Pilar Calatayud, M.; Goya, G. F.; Sánchez, F. H. Determination of the Blocking Temperature of Magnetic Nanoparticles: The Good, the Bad, and the Ugly. *J. Appl. Phys.* **2015**, *118*, 184304.

(48) Livesey, K. L.; Ruta, S.; Anderson, N. R.; Baldomir, D.; Chantrell, R. W.; Serantes, D. Beyond the Blocking Model to Fit Nanoparticle ZFC/FC Magnetisation Curves. *Sci. Rep.* **2018**, *8*, 11166.

(49) Frandsen, C.; Lefmann, K.; Lebech, B.; Bahl, C. R. H.; Brok, E.; Ancoña, S. N.; Theil Kuhn, L.; Keller, L.; Kasama, T.; Gontard, L. C.; Mørup, S. Spin Reorientation in α-Fe_2O_3 Nanoparticles Induced by Interparticle Exchange Interactions in α-

Fe_2O_3/NiO Nanocomposites. *Phys. Rev. B: Condens. Matter Mater. Phys.* **2011**, *84*, 214435.

(50) Normile, P. S.; Andersson, M. S.; Mathieu, R.; Lee, S. S.; Singh, G.; De Toro, J. A. Demagnetization Effects in Dense Nanoparticle Assemblies. *Appl. Phys. Lett.* **2016**, *109*, 152404.

(51) Andersson, M. S.; De Toro, J. A.; Lee, S. S.; Normile, P. S.; Nordblad, P.; Mathieu, R. Effects of the Individual Particle Relaxation Time on Superspin Glass Dynamics. *Phys. Rev. B: Condens. Matter Mater. Phys.* **2016**, *93*, 054407.

(52) Mathieu, R.; Jönsson, P.; Nam, D. N. H.; Nordblad, P. Memory and Superposition in a Spin Glass. *Phys. Rev. B: Condens. Matter Mater. Phys.* **2001**, *63*, 092401.

(53) Jönsson, P.; Mathieu, R.; Nordblad, P.; Yoshino, H.; Katori, H.; Ito, A. Nonequilibrium Dynamics of Spin Glasses: Examination of the Ghost Domain Scenario. *Phys. Rev. B: Condens. Matter Mater. Phys.* **2004**, *70*, 174402.

(54) Sahoo, S.; Petracic, O.; Kleemann, W.; Nordblad, P.; Cardoso, S.; Freitas, P. P. Aging and Memory in a Superspin Glass. *Phys. Rev. B: Condens. Matter Mater. Phys.* **2003**, *67*, 214422.

(55) Östh, M.; Hérisson, D.; Nordblad, P.; De Toro, J. A.; Riveiro, J. M. Ageing and Memory Effects in a Mechanically Alloyed Nanoparticle System. *J. Magn. Magn. Mater.* **2007**, *313*, 373–377.

(56) Bert, F.; Dupuis, V.; Vincent, E.; Hammann, J.; Bouchaud, J. Spin Anisotropy and Slow Dynamics in Spin Glasses. *Phys. Rev. Lett.* **2004**, *92*, 167203.

(57) Margaris, G.; Trohidou, K. N.; Nogués, J. Mesoscopic Model for the Simulation of Large Arrays of Bi-Magnetic Core/Shell Nanoparticles. *Adv. Mater.* **2012**, *24*, 4331–4336.

(58) Parker, D.; Dupuis, V.; Ladieu, F.; Bouchaud, J.-P.; Dubois, E.; Perzynski, R.; Vincent, E.; Vincent, E. Spin Glass Behavior in an Interacting γ-Fe_2O_3 Nanoparticle System. *Phys. Rev. B: Condens. Matter Mater. Phys.* **2008**, *77*, 104428.

(59) De Toro, J. A.; López De La Torre, M. A.; Riveiro, J. M.; Beesley, A.; Goff, J. P.; Thomas, M. F. Critical Spin-Glass Dynamics in a Heterogeneous Nanogranular System. *Phys. Rev. B: Condens. Matter Mater. Phys.* **2004**, *69*, 224407.

(60) Alonso, J.; Fdez-Gubieda, M. L.; Barandiarán, J. M.; Svalov, A.; Fernández Barquín, L.; Alba Venero, D.; Orue, I. Crossover from Superspin Glass to Superferromagnet in Fe_xAg_{100-x} Nanostructured Thin Films ($20 \leq x \leq 50$). *Phys. Rev. B: Condens. Matter Mater. Phys.* **2010**, *82*, 054406.

(61) Nogués, J.; Schuller, I. K. Exchange Bias. *J. Magn. Magn. Mater.* **1999**, *192*, 203–232.

(62) Kodama, R. H.; Berkowitz, A. E.; McNiff, E. J.; Foner, S. Surface Spin Disorder in $NiFe_2O_4$ Nanoparticles. *Phys. Rev. Lett.* **1996**, *77*, 394–397.

(63) Phan, M.-H.; Alonso, J.; Khurshid, H.; Lampen-Kelley, P.; Chandra, S.; Stojak Repa, K.; Nemati, Z.; Das, R.; Iglesias, Ó.; Srikanth, H. Exchange Bias Effects in Iron Oxide-Based Nanoparticle Systems. *Nanomaterials* **2016**, *6*, 221–251.

(64) De Toro, J. A.; Vasilakaki, M.; Lee, S. S.; Andersson, M. S.; Normile, P. S.;

Yaacoub, N.; Murray, P.; Sánchez, E. H.; Muñiz, P.; Peddis, D.; Mathieu, R.; Liu, K.; Geshev, J.; Trohidou, K. N.; Nogués, J. Remanence Plots as a Probe of Spin Disorder in Magnetic Nanoparticles. *Chem. Mater.* **2017**, *29*, 8258–8268.

(65) Poudyal, N.; Ping Liu, J. Advances in Nanostructured Permanent Magnets Research. *J. Phys. D: Appl. Phys.* **2013**, *46*, 043001.

(66) Fullerton, E. E.; Jiang, J. S.; Bader, S. D. Hard/Soft Magnetic Heterostructures: Model Exchange-Spring Magnets. *J. Magn. Magn. Mater.* **1999**, *200*, 392–404.

(67) López-Ortega, A.; Estrader, M.; Salazar-Alvarez, G.; Roca, A. G.; Nogués, J. Applications of Exchange Coupled Bi-Magnetic Hard/Soft and Soft/Hard Magnetic Core/Shell Nanoparticles. *Phys. Rep.* **2015**, *553*, 1–32.

(68) Mørup, S. Superparamagnetism and Spin Glass Ordering in Magnetic Nanocomposites. *Europhys. Lett.* **1994**, *28*, 671–676.

(69) Yerazunis, S.; Cornell, S. W.; Wintner, B. Dense Random Packing of Binary Mixtures of Spheres. *Nature* **1965**, *207*, 835–837.

(70) Stoner, E. C.; Wohlfarth, E. P. A Mechanism of Magnetic Hysteresis in Heterogeneous Alloys. *Philos. Trans. R. Soc., A* **1948**, *826*, 599–642.

(71) Jones, H. E.; Bissell, P. R.; Chantrell, R. W. The Dependence of Coercivity and Remanence on Dispersion Concentration in Fine Particle Systems. *J. Magn. Magn. Mater.* **1990**, *83*, 445–446.

(72) Néel, L. Le Champ Coercitif d'une Poudre Ferromagnetique Cubique a Grains

Anisotropes. *C. R. Seances Acad. Sci., Vie Acad.* **1947**, *224*, 1550–1551.

(73) Wohlfarth, E. P. The Effect of Particle Interaction on the Coercive Force of Ferromagnetic Micropowders. *Proc. R. Soc. London. Ser. A, Math. Phys.* **1955**, *232*, 208–227.

(74) Tan, R. P.; Lee, J. S.; Cho, J. U.; Noh, S. J.; Kim, D. K.; Kim, Y. K. Numerical Simulations of Collective Magnetic Properties and Magnetoresistance in 2D Ferromagnetic Nanoparticle Arrays. *J. Phys. D: Appl. Phys.* **2010**, *43*, 165002.

(75) Alonso, J. J.; Allés, B.; Russier, V. Phase Diagram for Ensembles of Random Close-Packed Ising-like Dipoles as a Function of Texturation. *Phys. Rev. B: Condens. Matter Mater. Phys.* **2019**, *100*, 134409.

(76) Stearns, M. B.; Cheng, Y. Determination of Para- and Ferromagnetic Components of Magnetization and Magnetoresistance of Granular Co/Ag Films (Invited). *J. Appl. Phys.* **1994**, *75*, 6894–6899.

(77) Sarkar, T.; Muscas, G.; Barucca, G.; Locardi, F.; Varvaro, G.; Peddis, D.; Mathieu, R. Tunable Single-Phase Magnetic Behavior in Chemically Synthesized $AFeO_3$-MFe_2O_4 (A = Bi or La, M = Co or Ni) Nanocomposites. *Nanoscale* **2018**, *10*, 22990–23000.

(78) Alben, R.; Becker, J. J.; Chi, M. C. Random Anisotropy in Amorphous Ferromagnets. *J. Appl. Phys.* **1978**, *49*, 1653–1658.

(79) Herzer, G. The Random Anisotropy Model. In *Properties and Application of Nanocrystalline Alloys from Amorphous Precursors*; Idzikowski, B., Švec, P.,

Miglierini, M., Eds.; Springer Netherlands, 2005; Vol. 184, pp 15–34.

(80) Nunes, W. C.; Socolovsky, L. M.; Denardin, J. C.; Cebollada, F.; Brandl, A. L.; Knobel, M. Role of Magnetic Interparticle Coupling on the Field Dependence of the Superparamagnetic Relaxation Time. *Phys. Rev. B: Condens. Matter Mater. Phys.* **2005**, *72*, 212413.

(81) Knobel, M.; Nunes, W. C.; Winnischofer, H.; Rocha, T. C. R.; Socolovsky, L. M.; Mayorga, C. L.; Zanchet, D. Effects of Magnetic Interparticle Coupling on the Blocking Temperature of Ferromagnetic Nanoparticle Arrays. *J. Non-Cryst. Solids* **2007**, *353*, 743–747.

(82) Muscas, G.; Concas, G.; Laureti, S.; Testa, A. M.; Mathieu, R.; De Toro, J. A.; Cannas, C.; Musinu, A.; Novak, M. A.; Sangregorio, C.; Lee, S. S.; Peddis, D. The Interplay between Single Particle Anisotropy and Interparticle Interactions in Ensembles of Magnetic Nanoparticles. *Phys. Chem. Chem. Phys.* **2018**, *20*, 28634–28643.

(83) Muscas, G.; Jovanović, S.; Vukomanović, M.; Spreitzer, M.; Peddis, D. Zn-Doped Cobalt Ferrite: Tuning the Interactions by Chemical Composition. *J. Alloys Compd.* **2019**, *796*, 203–209.

(84) Weissmüller, J.; Michels, A.; Barker, J. G.; Wiedenmann, A.; Erb, U.; Shull, R. D. Analysis of the Small-Angle Neutron Scattering of Nanocrystalline Ferromagnets Using a Micromagnetics Model. *Phys. Rev. B: Condens. Matter Mater. Phys.* **2001**, *63*, 214414.

(85) Michels, A.; Viswanath, R. N.; Barker, J. G.; Birringer, R.; Weissmüller, J. Range of Magnetic Correlations in Nanocrystalline Soft Magnets. *Phys. Rev. Lett.* **2003**, *91*, 267204.

(86) Aslibeiki, B.; Kameli, P.; Salamati, H.; Concas, G.; Fernandez, M. S.; Talone, A.; Muscas, G.; Peddis, D. Co-Doped $MnFe_2O_4$ Nanoparticles : Magnetic Anisotropy and Interparticle Interactions. *Beilstein J. Nanotechnol.* **2019**, *10*, 856–865.

(87) Giuntini, D.; Torresani, E.; Chan, K. T.; Blankenburg, M.; Saviot, L.; Bor, B.; Domènech, B.; Shachar, M.; Müller, M.; Olevsky, E. A.; Garay, J. E.; Schneider, G. A. Iron Oxide-Based Nanostructured Ceramics with Tailored Magnetic and Mechanical Properties: Development of Mechanically Robust, Bulk Superparamagnetic Materials. *Nanoscale Adv.* **2019**, *1*, 3139–3150.

(88) Abelson, A.; Qian, C.; Salk, T.; Luan, Z.; Fu, K.; Zheng, J. G.; Wardini, J. L.; Law, M. Collective Topo-Epitaxy in the Self-Assembly of a 3D Quantum Dot Superlattice. *Nat. Mater.* **2020**, *19*, 49–55.

(89) Cichelero, R.; Harres, A.; Sossmeier, K. D.; Schmidt, J. E.; Geshev, J. Magnetic Interactions in Exchange-Coupled yet Unbiased IrMn/NiCu Bilayers. *J. Phys.: Condens. Matter* **2013**, *25*, 426001.

(90) Vasilakaki, M.; Margaris, G.; Peddis, D.; Mathieu, R.; Yaacoub, N.; Fiorani, D.; Trohidou, K. Monte Carlo Study of the Superspin Glass Behavior of Interacting Ultrasmall Ferrimagnetic Nanoparticles. *Phys. Rev. B: Condens. Matter Mater. Phys.* **2018**, *97*, 094413.

(91) Vasilakaki, M.; Trohidou, K. N.; Peddis, D.; Fiorani, D.; Mathieu, R.; Hudl, M.; Nordblad, P.; Binns, C.; Baker, S. Memory Effects on the Magnetic Behavior of Assemblies of Nanoparticles with Ferromagnetic Core/Antiferromagnetic Shell Morphology. *Phys. Rev. B: Condens. Matter Mater. Phys.* **2013**, *88*, 140402.

(92) Srivastava, C. M.; Srinivasan, G.; Nanadikar, N. G. Exchange Constants in Spinel Ferrites. *Phys. Rev. B: Condens. Matter Mater. Phys.* **1979**, *19*, 499–508.

(93) Linderoth, S.; Hendriksen, P. V; Bødker, F.; Wells, S.; Davies, K.; Charles, S. W.; Mørup, S. On Spin-Canting in Maghemite Particles. *J. Appl. Phys.* **1994**, *75*, 6583–6585.

(94) Kaiser, R.; Miskolczy, G. Magnetic Properties of Stable Dispersions of Subdomain Magnetite Particles. *J. Appl. Phys.* **1970**, *41*, 1064–1072.

(95) Mazo-Zuluaga, J.; Restrepo, J. Monte Carlo Study of the Bulk Magnetic Properties of Magnetite. *Physica B* **2004**, *354*, 20–26.

(96) Ntallis, N.; Vasilakaki, M.; Peddis, D.; Trohidou, K. N. Effect of Organic Coating on the Charge Distribution of $CoFe_2O_4$ Nanoparticles. *J. Alloys Compd.* **2019**, *796*, 9–12.

(97) Salazar-Alvarez, G.; Qin, J.; Šepelák, V.; Bergmann, I.; Vasilakaki, M.; Trohidou, K. N.; Ardisson, J. D.; Macedo, W. A. A.; Mikhaylova, M.; Muhammed, M.; Baró, M. D.; Nogués, J. Cubic *versus* Spherical Magnetic Nanoparticles: The Role of Surface Anisotropy. *J. Am. Chem. Soc.* **2008**, *130*, 13234–13239.

(98) Vasilakaki, M.; Ntallis, N.; Yaacoub, N.; Muscas, G.; Peddis, D.; Trohidou, K. N.

Optimising the Magnetic Performance of Co Ferrite Nanoparticles *via* Organic Ligand Capping. *Nanoscale* **2018**, *10*, 21244–24253.

(99) Mørup, S.; Topsøe, H.; Clausen, B. S. Magnetic Properties of Microcrystals Studied by Mössbauer Spectroscopy. *Phys. Scr.* **1982**, *25*, 713–719.

(100) Ntallis, N.; Peyre, V.; Perzynski, R.; Dubois, E.; Trohidou, K. N. Charge Distribution on the Water/γ-Fe_2O_3 Interface. *J. Magn. Magn. Mater.* **2019**, *484*, 74–82.

(101) Pisane, K. L.; Singh, S.; Seehra, M. S. Unusual Enhancement of Effective Magnetic Anisotropy with Decreasing Particle Size in Maghemite Nanoparticles. *Appl. Phys. Lett.* **2017**, *110*, 222409.

(102) De Montferrand, C.; Lalatonne, Y.; Bonnin, D.; Lièvre, N.; Lecouvey, M.; Monod, P.; Russier, V.; Motte, L. Size-Dependent Nonlinear Weak-Field Magnetic Behavior of Maghemite Nanoparticles. *Small* **2012**, *8*, 1945–1956.

ToC Figure

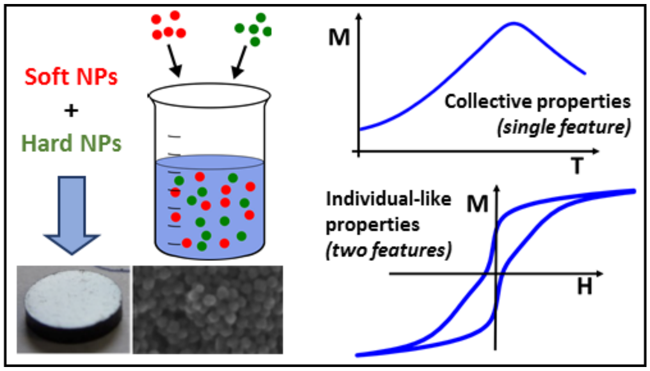

Supporting information for

Simultaneous individual and dipolar collective properties in binary assemblies of magnetic nanoparticles

Elena H. Sánchez[1], Marianna Vasilakaki[2], Su Seong Lee[3], Peter S. Normile[1], Giuseppe Muscas[4], Massimiliano Murgia[1,5], Mikael S. Andersson[6,7], Gurvinder Singh[8], Roland Mathieu[6], Per Nordblad[6], Pier Carlo Ricci[5], Davide Peddis[9,10], Kalliopi N. Trohidou[2], Josep Nogués[11,12], José A. De Toro[1]

[1] Instituto Regional de Investigación Científica Aplicada (IRICA) and Departamento de Física Aplicada, Universidad de Castilla-La Mancha 13071 Ciudad Real, Spain
[2] Institute of Nanoscience and Nanotechnology, NCSR "Demokritos", 153 10 Agia Paraskevi, Attiki, Greece
[3] Institute of Bioengineering and Nanotechnology, 31 Biopolis Way, The Nanos, Singapore 138669, Singapore
[4] Department of Physics and Astronomy, Uppsala University, Box 516, SE-751 20, Uppsala, Sweden
[5] Dipartimento di Fisica, Universitá degli Studi di Cagliari, S.P. Monserrato-Sestu Km 0,700, 09042 Monserrato (CA), Italy
[6] Department of Engineering Sciences, Uppsala University, Box 534, SE-751 21 Uppsala, Sweden
[7] Department of Chemistry and Chemical Engineering, Chalmers University of Technology, SE-412 96 Göteborg, Sweden
[8] School of Aerospace, Mechanical and Mechatronic Engineering, University of Sydney, Sydney, NSW 2008, Australia
[9]Università degli Studi di Genova, Dipartimento di Chimica e Chimica Industriale, Via Dodecaneso 31, 1-16146 Genova, Italy
[10]Istituto di Structura della Materia-CNR, 00015 Monterotondo Scalo (RM), Italy
[11] Catalan Institute of Nanoscience and Nanotechnology (ICN2), CSIC and BIST, Campus UAB, Bellaterra, 08193 Barcelona, Spain
[12] ICREA, Pg. Lluís Companys 23, 08010 Barcelona, Spain

On the nature of the interparticle interactions

The discussion in the main text has overlooked the possibility of interparticle superexchange. It is rather counterintuitive that an indirect exchange mediated by oxygen could propagate between metal ions in different particles, even if the NPs are essentially bare and *touching*. Yet, Frandsen et al. proved this to be the case between NiO antiferromagnetic NPs; however they showed that this was allowed by an exceptional crystalline coherence from particle to particle stemming from the synthesis method (which permitted the particles alignment) and the elongated shape of the NPs.[1] Nonetheless, some of us have recently found some indications of interparticle exchange in small maghemite nanoparticles without surface spin disorder and thus showing a negligible exchange bias field.[2] In the present study, the only NPs falling under such description are the maghemite particles used as LA component in the M2 series. Assuming an effective superexchange between them, the introduction of Co-doped particles in the M2 samples would reduce the number of LA-LA contacts and thus the average indirect exchange, which would therefore vary in the same way as the dipolar interaction strength (indicated by the arrow in Figure 6a2). Thus, the increasing T_{MAX} with x (proportion of HA particles) shown in that panel cannot be understood but in terms of the increasing local anisotropy. In short, even if superexchange interactions exist between the 6.8 nm particles, this would not affect any of the discussion.

On the evaluation of the *anisotropy energy contrast*

The difference in anisotropy between the constituent particles in the two series is quatified through the *anisotropy energy contrast*, AEC, defined as the ratio of the blocking temperatures of the two types of particles in the composite, $T_{B,HA}/T_{B,LA}$. The blocking temperature is often and most simply taken as the peak temperature in a low-field $M_{ZFC}(T)$ curve, which yields the AEC values cited in the main text (≈ 1.6 and 8.2 for series M1 and M2, respectively). However, this approximation systematically overestimates the average blocking temperature, which is obtained more rigorously from the maximum slope of the $M_{TRM}(T)$ curve [in turn equivalent to the difference $M_{FC}(T)$ - $M_{FC}(T)$]. From this definition, however, very similar AEC ratios are obtained (≈ 1.8 and 8.1 for series M1 and M2, respectively). Nonetheless, it is worth noticing that the latter AEC value for the M1 series is closer to the volume ratio between the constituent particles (≈ 2.0), which reduces the inferred contribution of the surface anisotropy to the energy barrier of the LA particles (still, however, larger than that in the HA particles, as the AEC value is still smaller than the volume ratio).

Experimental vs *superposition* ZFC loops in series M2

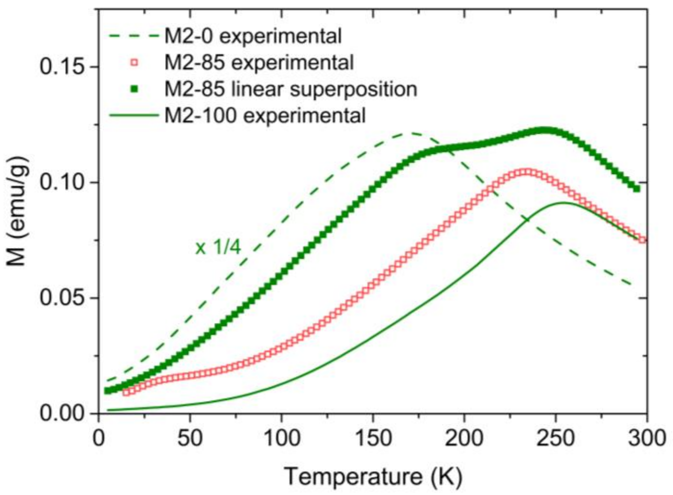

Figure S1. Comparison of the zero-field-cooled (ZFC) curve measured in H = 5 Oe for sample M2-85 (open symbols, same as in Figure 2) and the corresponding linear superposition of the ZFC curves of the end members of the series, i.e., 0.85×ZFC(M2-100) + 0.15×ZFC(M2-0) (filled symbols). Note that the selected example, x = 85, yields comparable peaks in the superposition due to the lower initial susceptibility of the hard particles in M2-100.

Low-temperature anomaly in the M2 series: ac susceptibility

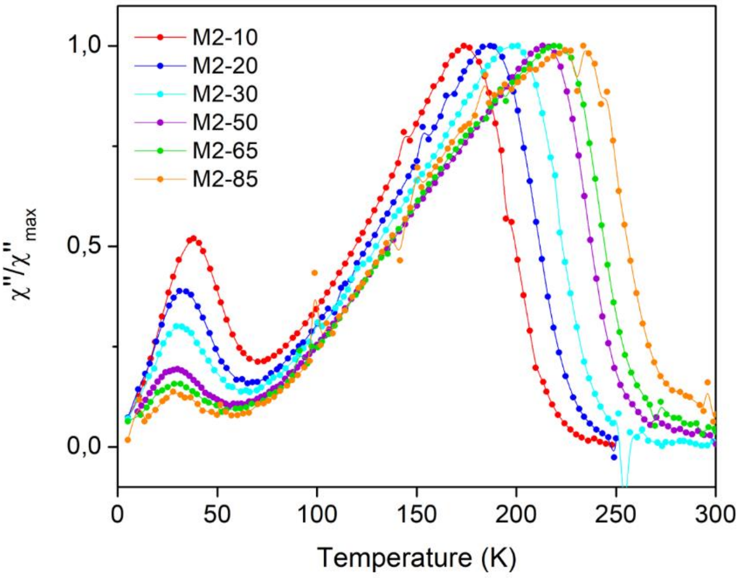

Figure S2. Temperature dependence of the normalized absorption component of the ac susceptibility at 10 Hz of all the *binary* compacts in series M2. A peak (with decreasing relative intensity with the HA-NPs proportion) is observed at the position of the low-temperature hump in the ZFC curves (see Figure 2 in the main text).

Room temperature loops and Langevin fits of silica-coated maghemite and Co-doped particles mixed in series M2

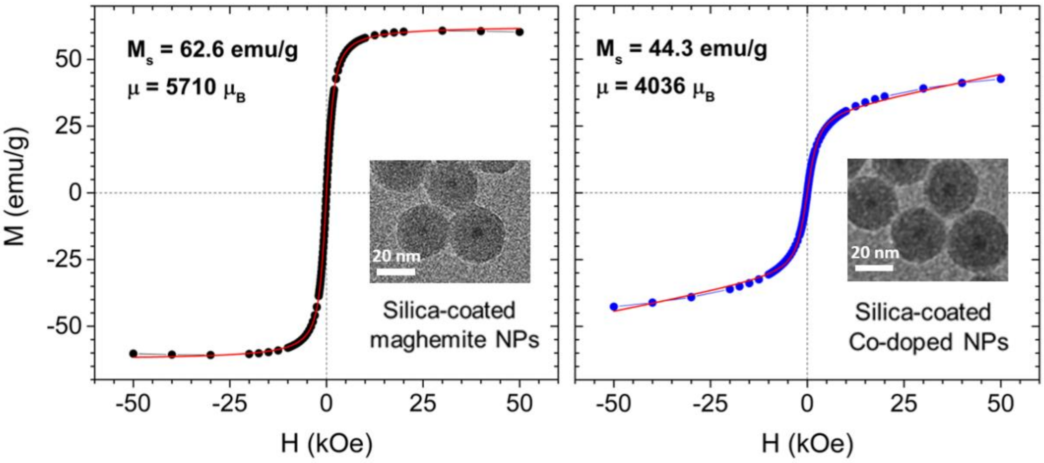

Figure S3. Room temperature response of magnetically dilute compacts (achieved by coating the cores with a thick silica layer, see insets) of the constituent nanoparticles in the M2 series (pure and Co-doped maghemite). The red lines are fits to a simple Langevin function, yielding the indicated effective NP moment (μ) and saturation magnetization (M_S) values. Note the close similarity between the ratios of these parameters ($\mu/M_S = V$) in each case, confirming that the magnetic cores have indeed the same volume.

Simulations of the blocking temperature, T_{MAX}, and coercivity, H_C, of the M1 series.

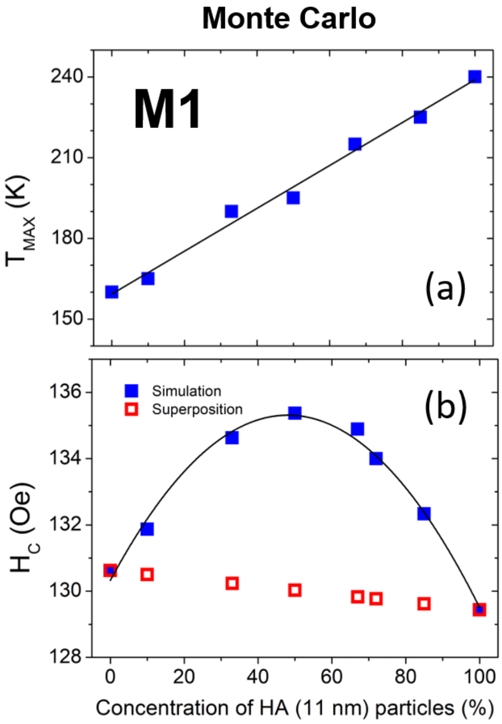

Figure S4. Dependence on the concentration of HA particles of the ZFC peak temperature, T_{MAX} (a), and the coercivity, H_C (b), resulting from Monte Carlo simulations of the M1 series. The open symbols in panel (b) correspond to values extracted from loops calculated as superpositions of the loops simulated for the end members of the M1 series. The lines are linear (a) and quadratic (b) fits to the data, respectively.

Monte Carlo: the model and examples of simulated curves

For the numerical study of the mixtures in the M1 and M2 series, we use the Monte Carlo simulation technique and the Metropolis algorithm.[3] We consider dense assemblies of spherical nanoparticles with diameter d, with a particle concentration c = 60%, randomly placed at the nodes of a simple cubic lattice with lattice characteristic lengths L_x, L_y, L_z with $L_x = L_y = L_z = 10\alpha$. The parameter α is defined as the smallest inter-particle distance equal to the particle diameter.

The small size of the nanoparticles results to a significant surface contribution in their magnetic behavior. Therefore, we use a 3-spin mesoscopic model[4] to simulate each nanoparticle with a core/surface morphology. Each nanoparticle is described by three classical spin vectors: one for the core $\mathbf{s}_{1i}$ and two for the surface layer $\mathbf{s}_{2i}$ and $\mathbf{s}_{3i}$ with i = 1,…,N (N is the total number of nanoparticles in the assembly). The magnetic moment for each nanoparticle's region is $m_n = M_nV_n / M_sV$, where n = 1 for the core and n = 2, 3 for the "up" and "down" surface layer sublattices. V_n and M_n are the volume and the saturation magnetization of the core, the "up" and the "down" surface sublattice regions, M_S and V are the saturation magnetisation and the total volume of the particle. Each spin has a uniaxial easy anisotropy axis randomly oriented. The total energy of the N nanoparticles system is:[5]

$$\begin{aligned}
E = &-\frac{1}{2}\sum_{i=1}^{N}\left[J_{c1}(\vec{s}_{1i}\cdot\vec{s}_{2i}) + J_{c2}(\vec{s}_{1i}\cdot\vec{s}_{3i}) + J_{srf}(\vec{s}_{2i}\cdot\vec{s}_{3i})\right] \\
&-\sum_{i=1}^{N} K_c V_1(\vec{s}_{1i}\cdot\hat{e}_{1i})^2 - \sum_{i=1}^{N} K_{srf}\left[V_2(\vec{s}_{2i}\cdot\hat{e}_{2i})^2 + V_3(\vec{s}_{3i}\cdot\hat{e}_{3i})^2\right] \\
&-\frac{1}{2}g\sum_{i,j=1,i\neq j}^{N}\Big(\sum_{n=1}^{3} m_{ni}\cdot\hat{s}_{ni}\Big)D_{ij}\Big(\sum_{n=1}^{3} m_{nj}\cdot\hat{s}_{nj}\Big) \\
&-\sum_{i=1}^{N}\sum_{n=1}^{3}\mu_0 H m_{ni}(\vec{s}_{ni}\cdot\hat{e}_h)
\end{aligned} \tag{Eq. 1}$$

The first energy term gives the intra-particle nearest-neighbor Heisenberg exchange interactions. Inside the angular brackets the exchange interaction between the core spin and the two surface spins (J_{c1} and J_{c2} are the intra-particle exchange coupling constants), and the exchange interaction between the surface spins (J_{srf} is the exchange coupling surface constant) are summed. The second and third energy terms give the anisotropy energy for the core (K_C) and the surface (K_{srf}) ($\hat{e}_{1i}$, $\hat{e}_{2i}$, $\hat{e}_{3i}$ being the anisotropy easy-axis directions). The forth energy term gives the dipolar interactions among all spins in the nanoparticles, D_{ij} is the dipolar interaction tensor.[4] The dipolar strength is defined as $g = \mu_0(M_sV)^2/4\pi d^3$. The last term is the Zeeman energy ($\hat{e}_h$ being the direction of the magnetic field H). We must note here that inter-particle exchange coupling is not included (see first section in this Supplementary Information).

It is important to emphasize that the different parameters used in the simulations are not fitting parameters. Our model starts from bulk parameters, which are known from the literature. Moreover, the volume of the core and the thickness of the surface layer are calculated from an atomic scale model of a nanoparticle with a spinel structure of size d and surface thickness 0.85 nm. This surface thickness corresponds approximately to a surface layer of one lattice constant of the bulk ferrite material [γ-Fe_2O_3 (~8.33 Å) and $CoFeO_4$ (~8.38 Å)] in agreement with experimental observations.[6,7]

To simplify the calculations, the exchange coupling energy and the magnetic anisotropy are normalized to the thermal energy k_BT (at temperature T = 10 K) to be dimensionless.
Since the purpose of the simulation is to establish that the origin of the effects that we infer from the experimental results are indeed valid, the different parameters used in the simulations are obtained from bulk values of the materials under study and by using experimental data:

(i) The exchange coupling parameters of the maghemite nanoparticles are estimated starting from their bulk values.[8] To set the mesoscopic parameters, we first perform atomic scale calculations for spherical nanoparticles with the inverse spinel crystalline structure of magnetite,[5,9–11] where in each fully occupied unit cell the iron ions are distributed in the tetrahedral sites (A-sublattice) and the octahedral sites (B-sublattice). Our atomic scale simulations show, for all the nanoparticle sizes, that in the core the B sublattice is the dominant one, so we set the core macrospin as a "B" spin. Consequently, based on Srivastava's values, we set $J_{c1} = J_{AB} = -25.5$ K for the exchange coupling between the core macrospin and that of the A surface sublattice, and $J_{c2} = J_{BB} = 15$ K for the exchange coupling between the core macrospin and the B surface sublattice.

In order to obtain the normalized exchange energy terms, j, e.g., $j_{c1} = ½×J_{AB}×S_A×S_B/k_BT$, one has to bear in mind that bulk maghemite has the structure $(Fe^{+3})_A\ [Fe^{+3}{}_{5/3}\ \square_{1/3}]\ _B$ where the symbol [] stands for ~20% vacancies and that the magnitude of the spin of Fe^{+3} are $S_A = S_B = 5/2$. Hence, since j_{c1} gives the interaction between A sites of the surface and B sites of the core, and vacancies exist only at B sites (i.e., A spins interact with 80% B spins), $j_{c1}= ½×J_{AB}×S_A×(S_B*80\%)/k_BT(10K) = -0.5×25.5×(5/2)×(5/2×0.8)/10 = -6.4$ Similarly, for j_{c2} (the B spins in the core interact with B spins in the surface B lattices) $j_{c2} = ½×15×0.8×(5/2)×(5/2)/10 = 3.8$.

From electronic structure calculations of maghemite and Co-ferrite nanoparticles it has been found that the j_{srf} values are close to the bulk ones, but the sign of J_{AA} is positive and its value is about ½ of the bulk one.[12,13] Following these results, we set $J_{surf\ AA} = 3.1$, $J_{surf\ BB} \approx J_{c2}$ and $J_{surf\ AB} \approx J_{c1}$. Moreover, in our atomic scale model for the three particle sizes we find that proportion (i.e., number of bonds over the total number of the surface bonds) of the coupling between AA, BB and AB sites are 0.1, 0.3, 0.6, respectively. The surface consists of two macrospins, therefore the mesoscopic exchange coupling at the surface j_{srf} has contributions from the couplings between AA, BB and AB surface bonds. Therefore, for the mesoscopic j_{srf} we take $j_{srf} = 0.1×3.1 + 0.3×3.8 - ½×0.6×6.4 \approx -0.5$. Note that the ½ in J_{AB} takes into account the double counting.

For the d = 6.8 nm Co-doped maghemite nanoparticles we use the values for the mesoscopic exchange coupling constants j_{c1} , j_{c2} , j_{srf} from the γ-Fe_2O_3 nanoparticles, since the experimental J_s of maghemite and $CoFe_2O_4$ are rather similar (i.e., $J_{BB} = 15$ K, $J_{AB} = -25.5$ K – γ-Fe_2O_3– vs. $J_{BB} = 18$ K, $J_{AB} = -25$ K –$CoFe_2O_4$–).[8]

(ii) The core anisotropy is estimated from the bulk value of the equivalent uniaxial anisotropy for maghemite, $K_C = K_{bulk}/12 = 4.7·10^4\ erg/cm^3/12 = 4·10^3\ erg/cm^3$ as suggested by S. Mørup and co-workers.[14] Thus, the parameter of the normalized core anisotropy $k_C= K_cV_c/k_BT(10K)$ for the d = 9 nm nanoparticle in MIX1 it becomes $k_{C\ (d=9)} = 0.5$. Using literature values for the surface anisotropy ($K_s \sim 0.035\ erg/cm^2$)[15] and the bulk value of the core anisotropy ($K_C = 4·10^3\ erg/cm^3$) and using the well-known expression for the effective anisotropy, $K_{eff} = K_C + 6K_s/d$, by setting $K_{srf} = 6K_s/d$ we get $K_{srf} /K_C \sim 60$. Consequently, in our calculations we take $k_{srf} = 30$ for the d = 9 nm.

In the larger nanoparticles, d = 11.5 nm, the core volume doubles that for the d = 9 nm case. Therefore, the effective anisotropy is $k_{C(d=11.5)} = 2×0.5 = 1$. In order to estimate the surface anisotropy $K_{srf,}$ we take into account the fact that as the nanoparticle size increases the surface contribution is reduced. Along these lines, experimental observations on maghemite nanoparticles gave an estimation of the reduction of the spin canting on the surface of the nanoparticles as the radius increases,[16] consequently the reduction of the spin canting results to the reduction of the surface sites where the surface anisotropy acts. We consider a ~0.33 reduction of the surface spin canting,[16] which results in a $(0.33)^2 \sim 0.1$ reduction of the corresponding surface area. Hence, we take $k_{srf(d=11.5)} = K_{srf(d=11.5)}V_{srf(d=11.5)}/k_BT(10K) = K_{srf(d=9)}×0.1×(1.67V_{srf(d=9)})/10K = (1/6)*k_{srf(d=9\ nm)} \approx 5$ in our reduced units.

Importantly, when these parameters are used in our model, they give $H_{C(d=9)}/H_{C(d=11.5)} \approx 1$ in agreement with the corresponding experimental values.

(iii) In the MIX2 series, for the maghemite nanoparticles of size d = 6.8 nm again, we take as reference the nanoparticle d = 9 nm, and we obtain $k_{C(d=6.8)}/k_{C(d=9.0)} \sim 0.3$, thus $k_{C(d=6.8)} = 0.17$. Given that $V_{srf(d=6.8)} = 0.54V_{srf(d=9)}$ and by taking into account the increase of the spin canting as the size decreases,[16] we find that $k_{srf\,(d=6.8\,)} = K_{srf(9)}\times 1.1\times 0.54V_{srf\,(d=9)}/k_BT(10K) \approx 15$.

For the 6.8 nm Co-doped particles, we consider that the core value of Co-doped maghemite particle is between the bulk values of the maghemite ($4\cdot 10^3$ erg/cm^3) and $CoFe_2O_4$ ($20\cdot 10^5$ erg/cm^3) and we set $K_c= 11\cdot 10^5$ erg/cm^3. Therefore the core anisotropy k_{C}-$_{Co\text{-}doped} = K_cV_c/k_BT(T=10K) = 275\times K_{c(6.8)maghemite}V_{c(6.8)maghemite}/10 = 275\times 0.17 \approx 50$.

For the surface anisotropy of Co-doped particles, we use the results of the Co doping effect on maghemite nanoparticles of a similar size of Fantechi and wo-workers.[17] Since $K_{eff} \sim 3\cdot 10^6$ erg/cm^3 is higher than the bulk value of $CoFe_2O_4$, we obtain $K_{srf} = K_{eff} - K_C = 3\cdot 10^6 - 1.1\cdot 10^6 = 1.9\cdot 10^6$ erg/cm^3, consequently, $K_{srf}/K_C \sim 2$. . Therefore, since $V_{srf} = 1.4V_C$, the surface anisotropy is taken as $k_{srf} = K_{srf}V_{srf}/k_BT(10K) = 150$.

Notably, when these parameters are introduced in the model they result in $H_{C\text{-}maghemite}/H_{C\text{-}Co\text{-}dop} \sim 0.05$, in good agreement with the experimental hysteresis loops.

(iv) The dipolar energy term, since each nanoparticle is described by three macrospins, one for the core and two for the two sublattices, is given by the expression:

$$E_{dip}=-\frac{1}{2}g\sum_{i,j=1,i\neq j}^{N}(m_{1i}\,\hat{s}_{1i}+m_{2i}\,\hat{s}_{2i}+m_{3i}\,\hat{s}_{3i})D_{ij}(m_{1j}\hat{s}_{1j}+m_{2j}\hat{s}_{2j}+m_{3j}\hat{s}_{3j}),$$

where m_1 is the core macrospin, and m_2 and m_3 are the surface macrospins and $\hat{s}_1, \hat{s}_2\,and\;\hat{s}_3$ are their corresponding unit vectors. Note that $\hat{s}_1 and\;\hat{s}_2$ are aligned parallel and they have antiparallel alignment with $\hat{s}_3$. Here D_{ij} is the dipolar tensor, that depends on the geometry of the assembly[4] and g is the dipolar strength defined as $g = \mu_0(M_sV)^2/4\pi d^3$ where M_s and V are the experimental values of the saturation magnetization and the volume of each particle.

The parameters m_1, m_2 and m_3 introduce a weight to each macrospin to account for the distribution of the volume saturation magnetizations in each region (core, surface) inside the particle. We call these parameters "the normalized magnetic moments" m_1, m_2 and m_3 and they are calculated as follows. From our atomic scale calculations, we determine the number of the A lattice sites N_{srfA} and the B lattice sites N_{srfB} at the surface and the uncompensated spins of the core which give the difference between the A and B lattice sites $N_{Core\,unc}= N_{CoreB} - N_{CoreA}$. For the surface the magnetic moments are calculated from the number of the surface spins at the B (S_BN_{srfB}) and the A (S_AN_{srfA}) sites, respectively, which are normalized by dividing them by the total magnetic moment coming from the uncompensated spins of the particle, that is $S_B(N_{Core\text{-}unc} + N_{srfB} - N_{srfA})$. Our calculations show that $m_2 = 1$ and $m_3 = 0.5$ in all cases because the ratios of uncompensated spins are similar for the three sizes. Since $m_{1i}\hat{s}_{1i}+m_{2i}\hat{s}_{2i}+m_{3i}\hat{s}_{3i}$ is a unit vector and $\hat{s}_{1i}, \hat{s}_{2i}, \hat{s}_{3i}$ are unit vectors, then $m_1+ m_2- m_3 = 1$, therefore $m_1 = 0.5$.

(v) For the calculation of the dipolar strength $g = \mu_0(M_sV)^2/4\pi d^3\,k_BT$ (T = 10 K) we have used the M_s from the measured hysteresis loops (Fig. 4 in the main text).

In the M1 series the dipolar strength g for the interaction between the small maghemite nanoparticles (d = 9.0 nm) is 17.4 and between the larger maghemite nanoparticles (d = 11.5 nm) 27. The mean dipolar strength for the interaction between small and large maghemite nanoparticles is taken g = c1· g1+ c2· g2 where c1 and c2 are the small and large maghemite nanoparticles concentrations, respectively. Thus, the corresponding dipolar strengths are g = 18.4, 19.3, 20.3, 22.3, 23.7 and 25.7 for c2 = 10%, 20%, 30%, 50%, 65% and 85%, respectively.

In the M2 series, for the assemblies of pure γ-Fe_2O_3 and Co-doped maghemite nanoparticles with d = 6.8 nm, the dipolar strength g is taken as 13.7 for the pairs of γ-Fe_2O_3 nanoparticles and 8.4 for the pairs of Co-doped nanoparticles, since the latter have lower M_S. For the interaction between maghemite and Co-doped nanoparticles in the binary M2 series we set a mean dipolar strength g = c1· g1+ c2· g2 where c1and c2 are the maghemite nanoparticles and the Co-doped maghemite nanoparticles concentrations, respectively (corresponding to g = 13.2, 12.6, 12.1, 11.1, 10.3 and 9.2 for c2 = 10%, 20%, 30%, 50%, 65% and 85%, respectively).

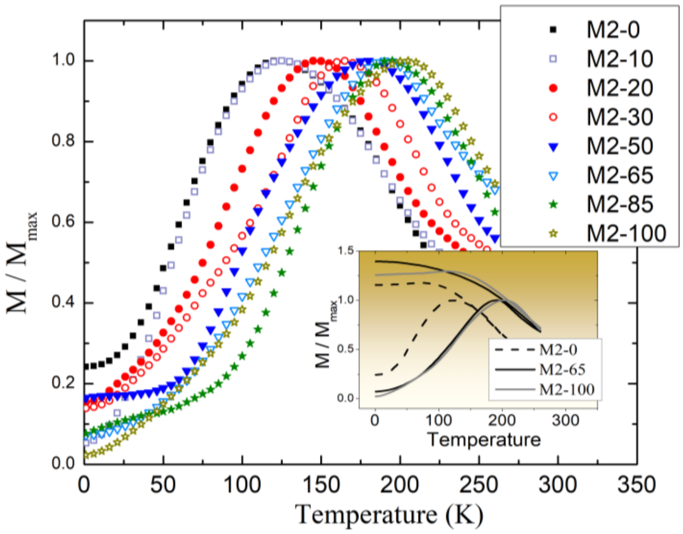

Figure S5. Simulated normalized ZFC curves for the M2 series. Shown in the inset are a few examples of the normalized FC/ZFC curves.

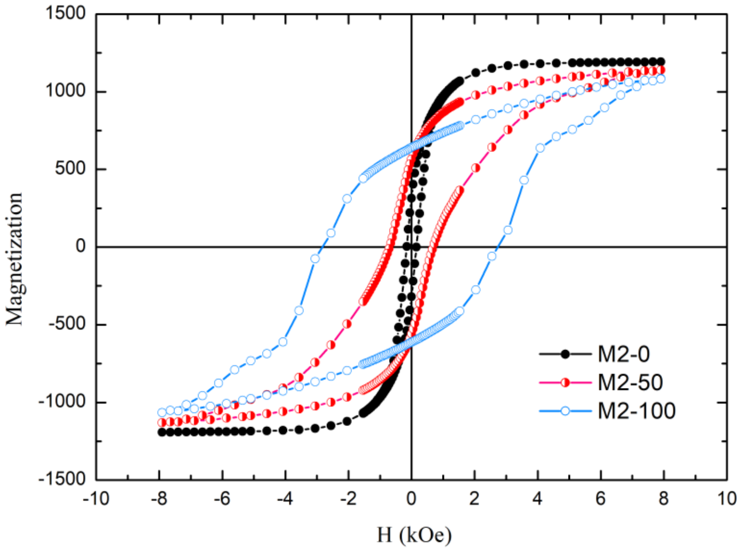

Figure S6. Simulated hysteresis loops for the end and middle members of the M2 series.

Random anisotropy model (RAM): analysis of T_B(H)

When the grain/particles size becomes smaller than the correlated volume of magnetic material, the effective anisotropy results from the average contribution of the individual interacting grains. This behaviour is described as the random anisotropy model (RAM) and it has been largely demonstrated for exchange interacting grains. Recently, some of us have successfully proposed the random anisotropy model to investigate the interplay between the individual particles anisotropy energy and the interparticle interactions for purely dipolar coupled particles.[18]

For an ensemble of non-interacting particles, the dependence of T_B on the applied field μ_0H is described by the law:[19,20]

$$T_B = \frac{K_a V_p}{k_B \ln\left(\frac{\tau_m}{\tau_0}\right)}\left[1 - \frac{\mu_0 H}{\mu_0 H_K}\right]^{\alpha} \quad \text{(Eq. 2)}$$

where K_a is the intrinsic anisotropy constant of the material, V_p the nanoparticle volume, $\alpha = 1.5$,[19] $\tau_m \sim 60$s (i.e., the typical experimental time in SQUID dc magnetization measurements), $\tau_0 = 10^{-11}$s (commonly used for ferromagnetic particles), $\mu_0 H_K$ the anisotropy field, and k_B the Boltzmann constant, $k_B = 1.38065\ 10^{-23}$ J/K.

For ensembles of interacting nanoparticles, their interactions extend over the magnetic correlation length (L_{corr})[21] that can be expressed as a function of the applied field:[20,22]

$$L_{corr} = D + \left[\frac{2A_{dip}}{M_S\, \mu_0 H + C}\right]^{1/2} \quad \text{(Eq. 3)}$$

where A_{dip} represents an effective dipolar interaction intensity.[23] The parameter C is needed to solve the divergence at $\mu_0 H = 0$ T. It considers the influence of particles concentration on interactions, assuming a value close to zero for clustered particles and the form $C \approx 2A_{eff} - M_S\, \mu_0 H$ for non-interacting ones.[19,20] In the framework of RAM, L_{corr} defines a correlation volume (V_N) where the effective anisotropy constant K_{eff} results from the fluctuations of the easy axes of the N grains within the correlation length, where the mean value varies as the square root of the number of independent contributions within the correlated volume: [23]

$$K_{eff} = \frac{K_a}{\sqrt{N}} \quad \text{(Eq. 4)}$$

where N can be defined as the ratio between the correlation volume and the volume of a single particle, considering the volume fraction x effectively occupied by the particles in the ensemble:

$$N = 1 + x\frac{(L_{corr}^3 - D^3)}{D^3} \quad \text{(Eq. 5)}$$

Therefore, we can define the volume of the cluster V_N as the effective volume of magnetic material interacting within the correlation length L_{corr}:

$$V_N = \frac{\pi}{6}[D^3 + x(L_{corr}^3 - D^3)] \quad \text{(Eq. 6)}$$

As the interparticle interactions increase, the correlation length expands and the anisotropy averages out over a larger volume, thus reducing its effective magnitude. On the other hand, an external magnetic field reduces the correlation length.[22] For an ensemble of interacting particles, one should consider the effective anisotropy field $\mu_0 H_K^N$ of the cluster of N correlated particles, which is linked to its effective average anisotropy K_{eff}:[19,20]

$$\mu_0 H_K^N = 2\frac{K_{eff}}{M_S} \quad \text{(Eq. 7)}$$

Finally, equation (Eq. 2) can be re-written by substituting K_a, V_p and H_K with the effective values for the cluster K_{eff}, V_N and H_K^N, respectively to define the field dependence of the effective blocking temperature of the NPs' ensemble:

$$T_B(\mathrm{H}) = \frac{K\frac{\pi}{6}\left[D^3 + x\left(L_{corr}^3 - D^3\right)\right]}{6\,k_B \ln\left(\frac{\tau_m}{\tau_0}\right)\sqrt{1 + x\frac{\left(L_{corr}^3 - D^3\right)}{D^3}}}\left[1 - \frac{\mu_0 H M_S\sqrt{1 + x\frac{\left(L_{corr}^3 - D^3\right)}{D^3}}}{2\mathrm{K}}\right]^{1.5} \qquad \text{(Eq. 8)}$$

The experimental values of $T_B(H)$ were extracted using FC/ZFC curves measured at different applied fields from the peak of the effective distribution of energy barriers, defined as:

$$f(T) \propto \frac{d(M_{ZFC} - M_{FC})}{dT} \qquad \text{(Eq. 9)}$$

Figure S7 report the *(M_{FC} - M_{ZFC})* curves and their negative derivative for samples M2-0 and M2-100, as well as the fitting of the experimental values of average blocking temperature to Eq. 8. The results of the fit for the M2-0, M2-10, M2-50, M2-85 and M2-100 samples are summarized in Table S1.

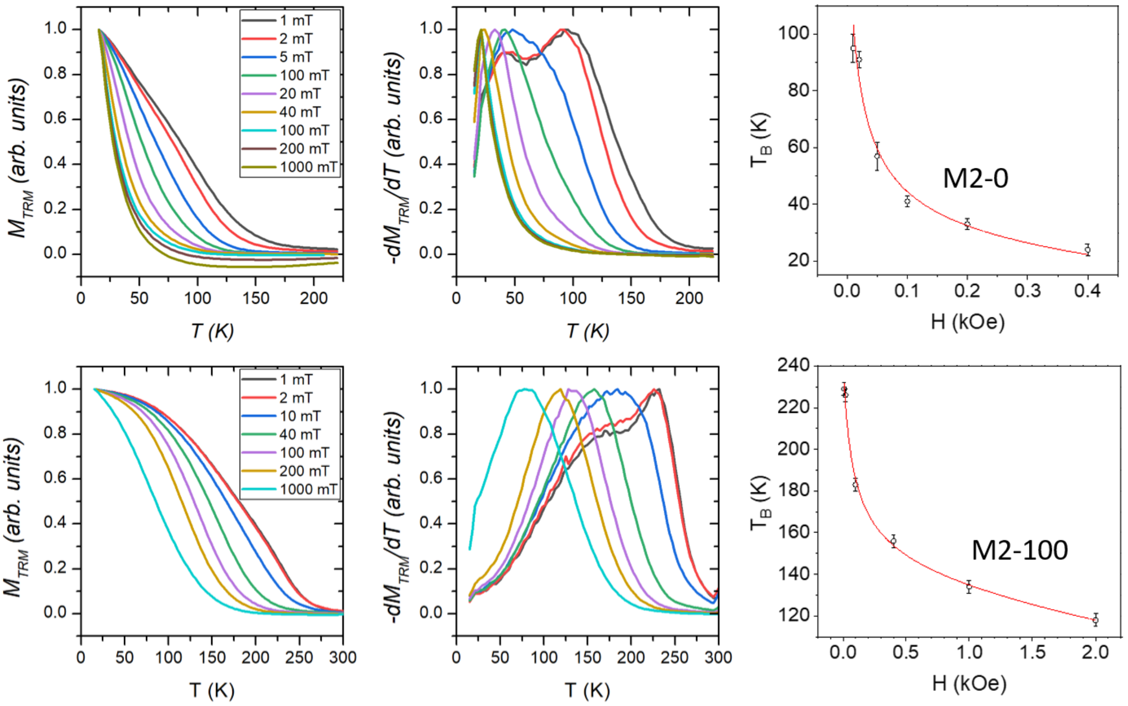

Figure S7. TRM curves (left), equivalent to (M_{FC} - M_{ZFC}), and its inverse derivative (middle) measured at different applied fields for samples M2-0 (upper panels) and M2-100 (lower panels). The field dependence of the effective average blocking temperature (peak value of the derivative) and its fit to Eq. 8 (red line) are shown in the right panels.

According to the RAM results, the magnetic properties of the pure maghemite particles in M2-0 are averaged over many particles, with L_{corr} about 36 nm, thus leading to collective behaviour, as also confirmed by the largest A_{dip} value. On the other hand, for the Co-doped maghemite nanoparticles (M2-100), L_{corr} is larger than the individual particle size (6.8 nm), but smaller than the diameter of a sphere containing two particles. Indeed, even if the particles are strongly coupled, the individual particle energy barrier will still dominate the magnetization reversal of this sample. The good agreement obtained between the intrinsic (particle) blocking temperature extracted from the RAM fit ($T_{B0} \propto K_a V$) and the values measured for the isolated maghemite and Co-doped particles (solid lines in Figure 2b) lends credibility to the RAM analysis.

Sample	**L_{corr} (nm)**	**A_{dip} (J m^{-1})**	**K_a (kJ m^{-3})**	**T_{B0} (K)**
M2-0	36(1)	1.1(8)e-13	45 (6)	21(5)
M2-10	13.2(5)	7(4)e-14	150 (10)	72(5)
M2-50	11.2(5)	1.3(4)e-14	243 (6)	114(5)
M2-85	10.8(5)	4.2(5)e-14	238 (2)	112(5)
M2-100	11.4(5)	1.9(6)e-14	272 (8)	150(5)

Table S1. The correlation length L_{corr} and the effective dipolar interaction strength A_{dip} are reported for several samples in the M2 series. In addition, the table shows the average intrinsic anisotropy and the corresponding blocking temperature, beyond interactions effects, extracted from the fit.

References

(1) Frandsen, C.; Lefmann, K.; Lebech, B.; Bahl, C. R. H.; Brok, E.; Ancoña, S. N.; Theil Kuhn, L.; Keller, L.; Kasama, T.; Gontard, L. C.; Mørup, S. Spin Reorientation in α-Fe_2O_3 Nanoparticles Induced by Interparticle Exchange Interactions in α-Fe_2O_3/NiO Nanocomposites. *Phys. Rev. B: Condens. Matter Mater. Phys.* **2011**, *84*, 214435.

(2) Andersson, M. S.; Mathieu, R.; Lee, S. S.; Normile, P. S.; Singh, G.; Nordblad, P.; Toro, J. A. De. Size-Dependent Surface Effects in Maghemite Nanoparticles and Its Impact on Interparticle Interactions in Dense Assemblies. *Nanotechnology* **2015**, *26*, 475703.

(3) Vasilakaki, M.; Trohidou, K. N.; Peddis, D.; Fiorani, D.; Mathieu, R.; Hudl, M.; Nordblad, P.; Binns, C.; Baker, S. Memory Effects on the Magnetic Behavior of Assemblies of Nanoparticles with Ferromagnetic Core/Antiferromagnetic Shell Morphology. *Phys. Rev. B: Condens. Matter Mater. Phys.* **2013**, *88*, 140402.

(4) Margaris, G.; Trohidou, K. N.; Nogués, J. Mesoscopic Model for the Simulation of Large Arrays of Bi-Magnetic Core/Shell Nanoparticles. *Adv. Mater.* **2012**, *24*, 4331–4336.

(5) Vasilakaki, M.; Margaris, G.; Peddis, D.; Mathieu, R.; Yaacoub, N.; Fiorani, D.; Trohidou, K. Monte Carlo Study of the Superspin Glass Behavior of Interacting Ultrasmall Ferrimagnetic Nanoparticles. *Phys. Rev. B: Condens. Matter Mater. Phys.* **2018**, *97*, 094413.

(6) Linderoth, S.; Hendriksen, P. V; Bødker, F.; Wells, S.; Davies, K.; Charles, S. W.; Mørup, S. On Spin-Canting in Maghemite Particles. *J. Appl. Phys.* **1994**, *75*, 6583–6585.

(7) Kaiser, R.; Miskolczy, G. Magnetic Properties of Stable Dispersions of Subdomain Magnetite Particles. *J. Appl. Phys.* **1970**, *41*, 1064–1072.

(8) Srivastava, C. M.; Srinivasan, G.; Nanadikar, N. G. Exchange Constants in Spinel Ferrites. *Phys. Rev. B: Condens. Matter Mater. Phys.* **1979**, *19*, 499–508.

(9) Mazo-Zuluaga, J.; Restrepo, J. Monte Carlo Study of the Bulk Magnetic Properties of

Magnetite. *Physica B* **2004**, *354*, 20–26.

(10) Ntallis, N.; Vasilakaki, M.; Peddis, D.; Trohidou, K. N. Effect of Organic Coating on the Charge Distribution of $CoFe_2O_4$ Nanoparticles. *J. Alloys Compd.* **2019**, *796*, 9–12.

(11) Salazar-Alvarez, G.; Qin, J.; Šepelák, V.; Bergmann, I.; Vasilakaki, M.; Trohidou, K. N.; Ardisson, J. D.; Macedo, W. A. A.; Mikhaylova, M.; Muhammed, M.; Baró, M. D.; Nogués, J. Cubic *versus* Spherical Magnetic Nanoparticles: The Role of Surface Anisotropy. *J. Am. Chem. Soc.* **2008**, *130*, 13234–13239.

(12) Vasilakaki, M.; Ntallis, N.; Yaacoub, N.; Muscas, G.; Peddis, D.; Trohidou, K. N. Optimising the Magnetic Performance of Co Ferrite Nanoparticles *via* Organic Ligand Capping. *Nanoscale* **2018**, *10*, 21244–24253.

(13) Ntallis, N.; Peyre, V.; Perzynski, R.; Dubois, E.; Trohidou, K. N. Charge Distribution on the Water/γ-Fe_2O_3 Interface. *J. Magn. Magn. Mater.* **2019**, *484*, 74–82.

(14) Mørup, S.; Topsøe, H.; Clausen, B. S. Magnetic Properties of Microcrystals Studied by Mössbauer Spectroscopy. *Phys. Scr.* **1982**, *25*, 713–719.

(15) Pisane, K. L.; Singh, S.; Seehra, M. S. Unusual Enhancement of Effective Magnetic Anisotropy with Decreasing Particle Size in Maghemite Nanoparticles. *Appl. Phys. Lett.* **2017**, *110*, 222409.

(16) De Montferrand, C.; Lalatonne, Y.; Bonnin, D.; Lièvre, N.; Lecouvey, M.; Monod, P.; Russier, V.; Motte, L. Size-Dependent Nonlinear Weak-Field Magnetic Behavior of Maghemite Nanoparticles. *Small* **2012**, *8*, 1945–1956.

(17) Fantechi, E.; Campo, G.; Carta, D.; Corrias, A.; de Julián Fernández, C.; Gatteschi, D.; Innocenti, C.; Pineider, F.; Rugi, F.; Sangregorio, C. Exploring the Effect of Co Doping in Fine Maghemite Nanoparticles. *J. Phys. Chem. C* **2012**, *116*, 8261–8270.

(18) Muscas, G.; Concas, G.; Laureti, S.; Testa, A. M.; Mathieu, R.; De Toro, J. A.; Cannas, C.; Musinu, A.; Novak, M. A.; Sangregorio, C.; Lee, S. S.; Peddis, D. The Interplay between Single Particle Anisotropy and Interparticle Interactions in Ensembles of Magnetic Nanoparticles. *Phys. Chem. Chem. Phys.* **2018**, *20*, 28634–28643.

(19) Knobel, M.; Nunes, W. C.; Winnischofer, H.; Rocha, T. C. R.; Socolovsky, L. M.; Mayorga, C. L.; Zanchet, D. Effects of Magnetic Interparticle Coupling on the Blocking Temperature of Ferromagnetic Nanoparticle Arrays. *J. Non-Cryst. Solids* **2007**, *353*, 743–747.

(20) Nunes, W. C.; Socolovsky, L. M.; Denardin, J. C.; Cebollada, F.; Brandl, A. L.; Knobel, M. Role of Magnetic Interparticle Coupling on the Field Dependence of the Superparamagnetic Relaxation Time. *Phys. Rev. B: Condens. Matter Mater. Phys.* **2005**, *72*, 212413.

(21) Weissmüller, J.; Michels, A.; Barker, J. G.; Wiedenmann, A.; Erb, U.; Shull, R. D. Analysis of the Small-Angle Neutron Scattering of Nanocrystalline Ferromagnets Using a

Micromagnetics Model. *Phys. Rev. B: Condens. Matter Mater. Phys.* **2001**, *63*, 214414.

(22) Michels, A.; Viswanath, R. N.; Barker, J. G.; Birringer, R.; Weissmüller, J. Range of Magnetic Correlations in Nanocrystalline Soft Magnets. *Phys. Rev. Lett.* **2003**, *91*, 267204.

(23) Herzer, G. The Random Anisotropy Model. In *Properties and Application of Nanocrystalline Alloys from Amorphous Precursors*; Idzikowski, B., Švec, P., Miglierini, M., Eds.; Springer Netherlands, 2005; Vol. 184, pp 15–34.